

LUDWIG-MAXIMILIANS-UNIVERSITÄT

FACULTY OF PHYSICS

Master's Thesis in Physics

A Molecular Lattice Clock



Christian Liedl

2018

LUDWIG-MAXIMILIANS-UNIVERSITÄT

FACULTY OF PHYSICS

Master's Thesis in Physics

A Molecular Lattice Clock

Eine Molekulare Gitter Uhr

Author: Christian Liedl
Submission Date: July 31, 2018



Primary Advisor:
Prof. Dr. Tanya Zelevinsky
Columbia University in the
City of New York

Secondary Advisor:
Prof. Dr. Immanuel Bloch
Ludwig-Maximilians-Universität
München

Acknowledgments

I'm very grateful to the Max Weber Programm Bayern and PROSA LMU for their financial support of my research year in New York. I would like to thank my advisor at LMU, Professor Immanuel Bloch, for agreeing to evaluate this thesis.

Many thanks to Professor Tanya Zelevinsky, for allowing me to participate in the exciting research conducted in her labs. I enjoyed the open and communicative environment in her group and I'm thankful for her great advice, which often helped push the experiments in the right direction.

Especially I want to thank Dr. Stanimir Kondov, who has guided my clumsy first steps as a scientist with great patience and has made the strontium experiment such a fun and exciting place. I thank him for always taking his time to share his vast knowledge of AMO physics, troubleshoot problems and discuss new and creative ideas.

Chih-Hsi Lee knows every single inch of the strontium experiment by heart and makes running this complicated machine look incredibly easy. I thank him for teaching me about the experiment and his great experimental skills, which were crucial for many results presented in this thesis.

I would like to thank Kon Leung for his help and advice on many projects. Our discussions often led me to a better understanding and I admire his thorough and analytical thinking.

Despite working on a different experiment, Rees McNally has often helped me make progress thanks to his creativity and all-round knowledge about basically everything that would ever be needed in an AMO lab. Thanks for always spreading scientific enthusiasm, the many laughs and crazy Friday afternoon ideas.

Many thanks also to Konrad Wenz and Dr. Geoffrey Iwata, for sharing their knowledge with me and making ZLab an incredible place to do research.

I thank the whole group for welcoming me and making me feel at home in New York City. I'm very excited to follow future ZLab discoveries and I'm very grateful for having been able to take part in this exciting journey.

I want to thank my friends for taking my mind off physics, alleviating any stress and frustration and for many great moments.

A special thanks goes to my parents and my brother, who have always encouraged me and offered advice. Thanks for the unconditional support and making my life so easy. Most importantly, I want to thank Mariel García Huiman for her never ending support and understanding and for making every day bright and joyful.

Abstract

Ultracold molecules provide a new and promising platform for studies of fundamental physics. Tight confinement of the homonuclear, diatomic molecule $^{88}\text{Sr}_2$ in an optical lattice allows for high precision two-photon spectroscopy of rovibrational levels. Such a molecular lattice clock is sensitive to possible variations of the electron-proton mass ratio, molecular QED effects and could enable searches for nano-scale deviations from Newtonian gravity. This thesis presents the development of the metrology system necessary to achieve Hz-level two-photon spectroscopy, adapting techniques originally designed for atomic single-photon clocks.

A new master clock laser is built to improve the stability of the metrology system. Spectral stability transfer between the clock lasers is achieved using a frequency comb to bridge a gap of 26 THz. Metrologically important light is distributed between remote locations using a fiber noise cancellation scheme featuring integrated intensity stabilization and supporting relative stability on the 10^{-18} level.

Several candidate clock pairs are located by employing Autler-Townes spectroscopy. By tuning the differential light shift near narrow polarizability resonances, state insensitive trapping is achieved, yielding a 400-fold improvement in coherence. Finally, Rabi oscillations are achieved across the ground state potential and current limitations on a preliminary linewidth of 160 Hz are discussed.

Contents

Acknowledgments	ii
Abstract	iii
1 Introduction	1
1.1 A Molecular Lattice Clock	1
1.2 Overview	3
2 Structure of $^{88}\text{Sr}_2$	5
2.1 Electronic Ground State	6
2.2 Excited States	6
2.3 Selection Rules	7
3 Production of Ultracold $^{88}\text{Sr}_2$ Groundstate Molecules	9
3.1 Laser Cooling of ^{88}Sr	9
3.2 Photoassociation	10
3.3 Imaging	11
4 Laser Stabilization	13
4.1 Clock Laser	13
4.1.1 Fabry-Perot Resonator	13
4.1.2 PDH Locking	19
4.1.3 Setup and Locking Procedure	20
4.1.4 Evaluation of the Locking Performance	24
4.2 Fiber Noise Cancellation and Intensity Stabilization	27
4.2.1 Setup	27
4.2.2 Evaluation of Cancellation Performance	29
4.3 Stability Transfer Using a Frequency Comb	32
4.3.1 Elastic Tape Model	32
4.3.2 Stability Transfer	33
4.3.3 CEO Subtraction	35
4.3.4 Metrology with a Frequency Comb	38

5 Autler-Townes Spectroscopy of Deeply Bound Ground States	41
5.1 Lambda Scheme	41
5.2 Binding Energies	44
6 Magic Wavelength Spectroscopy	47
6.1 Polarizability	47
6.2 Magic Wavelength	47
6.2.1 Off-Resonant Scattering	50
6.2.2 TA Pedestal	51
6.3 Current Limitations	51
7 Coherent Transfer	55
7.1 Rabi Oscillation	55
7.2 Lifetime Measurements	56
8 Summary and Outlook	59
A Appendix	63
A.1 A Unibody Littman Laser	63
A.2 Polarizability and Scattering Rate	65
List of Figures	67
List of Tables	69
Bibliography	71

1 Introduction

The standard model (SM) of particle physics has been tested to incredible precision using experiments in the entire spectrum of modern physics [1]. At the same time, it seems incomplete, as it struggles to incorporate gravity in its framework, explain the matter-antimatter imbalance, dark matter or dark energy.

Remarkably, dark matter and dark energy make up around 95 % of the energy in our universe [2]. With the discovery of the Higgs particle in 2012 [3], all particles in the SM have been observed, while it only explains 5 % of the energy in the universe.

This unsatisfying situation has sparked great efforts to detect new particles and observe physics beyond the SM. While direct searches typically involve collider experiments at energy scales of $\mathcal{O}(\text{TeV})$, one can also search for deviations in the low energy regime of ultracold atoms and molecules. Advances in atomic, molecular and optical (AMO) physics in the last two decades have led to ever increasing quantum control and precision, opening new pathways for tests of fundamental physics beyond the standard model [4]. This progress allows for unprecedented precision measurements. Atomic magnetometers can measure magnetic fields at the level of $10^{-15} \text{ THz}^{-1/2}$ [5] and the Laser Interferometer Gravitational-Wave Observatory (LIGO) is capable of detecting changes in length at $10^{-23} \text{ Hz}^{-1/2}$, which has led to the observation of gravitational waves in 2016 [6].

In particular, the development of optical atomic clocks has improved the accuracy of frequency metrology by three orders of magnitude in the last ten years [7]. The highest precision and stability is achieved using ultracold atoms in an optical lattice, yielding a fractional frequency uncertainty of 2×10^{-18} for ^{87}Sr [8].

Much of the research in our group has focused on adapting techniques originally developed for atomic clocks to molecules and establishing a new platform for tests of the fundamental laws governing the universe.

1.1 A Molecular Lattice Clock

A clock measures time based on a stable reference oscillator. For a simple clock, this reference could be the swinging of a pendulum. If complete isolation from the environment is achieved, this frequency standard should only depend on the fundamental

constants of physics that determine the frequency of the oscillator. For a pendulum, this is e.g. the gravitational constant G .¹

In the SM, all fundamental constants are indeed invariable, i.e. they don't change over time. However, several models beyond the SM suggest that the fundamental constants dynamically vary with time. These include e.g. string theories, discrete quantum gravity and loop quantum gravity [9].

How would one go about measuring these drifts? The measurement of a physical quantity usually relies on the comparison between the measured system and a reference that defines the unit. But what if the reference and thus the unit itself changes over time? For this reason, searches for drifts in fundamental constants concentrate on the two dimensionless constants in the SM: the fine structure constant α and the electron-proton mass ratio $\mu = \frac{m_e}{m_p}$.

These drifts can be searched for in a variety of astrophysical systems, reviewed in [10]. To detect present-day variations in the lab, one could compare different clock transitions which exhibit different dependencies on α and μ respectively. If the constants change, so will the ratio between the two transition frequencies. Atomic clocks possess a strong sensitivity for drifts in α . While μ can also be measured with atomic clocks, the resulting constraints cannot be separated model independently from α drifts [11].

In contrast, if one uses vibrational levels in the same electronic potential of a molecule, the clock transition is most sensitive to μ [12, 13]. By selecting two clock transitions with maximally different μ dependencies, one can directly measure μ drifts in a clean way, while the α dependence, as well as any intermediate clock drift essentially cancels out [14, 15].

Further prospects of a molecular clock could include improving constraints on the validity of nano-scale gravity and precise measurements of the potential can inform quantum chemical ab-initio calculations.

$^{88}\text{Sr}_2$ is an ideal choice for a molecular clock, since the vibrational levels are relatively immune to black body radiation due to selection rules. Furthermore, the lack of hyperfine structure makes the clock less sensitive to magnetic field fluctuations. Lastly, ^{88}Sr can be laser cooled to $\sim 1 \mu\text{K}$. With a subsequent photoassociation of the Sr dimers, it is possible to achieve Doppler- and recoil-free spectroscopy in an optical lattice.

¹For a pendulum, the eigenfrequency depends of course highly on the local gravitational environment.

1.2 Overview

The first two chapters describe the theoretical and experimental framework necessary to understand the experiments described in this thesis. Chapter 2 gives a short review on the molecular structure of $^{88}\text{Sr}_2$, while chapter 3 explains the experimental apparatus and how ultracold $^{88}\text{Sr}_2$ molecules are produced.

Chapter 4 describes the development of the metrology system: A new clock laser is built improving our metrological capability. Fiber noise cancellation is implemented to distribute the stable light between remote locations. Finally, the stability is transferred between Raman lasers to ensure the relative stability of the two clock lasers. In chapter 5, Autler-Townes spectroscopy of deeply bound vibrational states is presented. Once these prospective clock transitions are found, the inhomogeneous Stark broadening is eliminated by employing a magic wavelength technique, as discussed in chapter 6. The increased coherence allows us to coherently transfer molecules between vibrational levels. Chapter 7 describes Rabi oscillations across almost the entire ground state potential. Finally, the results of this thesis are summarized and a short outlook on the next steps towards the experiments outlined above is given.

2 Structure of $^{88}\text{Sr}_2$

This chapter provides a short review of the molecular structure of $^{88}\text{Sr}_2$ and will only focus on the cases relevant for the experiments described in this thesis. More detailed explanations can be found in [16, 17, 18, 19]. Let's consider the following Hamiltonian for the diatomic, homonuclear molecule:

$$\hat{H} = \hat{H}_e + \hat{H}_v + \hat{H}_r \quad (2.1)$$

In this simple picture, the electronic (\hat{H}_e), vibrational (\hat{H}_v) and rotational (\hat{H}_r) parts of the Hamiltonian are decoupled.

To first approximation, the electronic energy is given by the sum of the energies of the two atoms forming the molecule (atomic asymptote). The vibrational part can be described by a single quantum number v . The rotational part is the most complicated since it depends on the different couplings of spin and orbital angular momentum of the electrons and nuclei respectively. Note that the nuclear spin is 0 for $^{88}\text{Sr}_2$.

Molecular states are typically classified by different Hund's cases: Depending on the coupling of the angular momenta and spins, a different set of "good" quantum numbers is used to describe the state. One has to consider the interplay between the following operators:

- \hat{L} ($\hat{\Lambda}$): Electronic angular momentum
- \hat{S} ($\hat{\Sigma}$): Electronic spin
- $\hat{j}_e = \hat{L} + \hat{S}$ ($\hat{\Omega}$): Total electronic angular momentum
- \hat{R} : Rotational nuclear angular momentum
- $\hat{j} = \hat{R} + \hat{j}_e$: Total molecular angular momentum

where the Greek letters in brackets denote the projection onto the nuclear axis.

2.1 Electronic Ground State

The electronic ground state is best described by Hund's case a), in which \hat{L} is strongly coupled to the inter-nuclear axis and \hat{S} is strongly coupled to \hat{L} . A set of "good" quantum numbers is then given by Λ , Σ , Ω , J and S . The most common notation for molecules described by Hund's case a) is similar to the atomic spectroscopic notation:

$$^{2S+1}|\Lambda|_{\Omega,(g/u)}^{\pm} \quad (2.2)$$

where \pm indicates the sign of Λ and the subscript g/u (gerade/ungerade or even/odd) denotes the electronic parity, i.e. whether the wave function changes sign under reflection at a plane normal to the inter-nuclear axis. The values of Λ are labeled by the Greek letters Σ , Π , etc., in analogy to the atomic notation (S,P, etc.).

The electronic ground state is labeled as X and asymptotes to the $^1S_0 + ^1S_0$ atomic state, so that $L = S = J_e = \Omega = 0$, justifying the application of Hund's case a). The term symbol for the molecular ground state potential thus reads: $^1\Sigma_{0,g}^+$, where g and $+$ can be obtained by symmetry considerations, since the ^{88}Sr nucleus is bosonic.

To fully describe the state, one additionally has to specify the vibrational quantum number v and J . For symmetry reasons, only even J are allowed for the ground state. To simplify the notation, the rovibrational levels in the ground state will simply be labeled as $X(v, J, m_J)$ in this thesis. We will often omit m_J , especially when dealing with $J = 0$. It is also important to note that $v = 0$ is the most deeply bound state. When we consider weakly bound states near the atomic asymptote, it is common to use negative values for v , i.e. $v = -1$ denotes the most shallow bound state and is equivalent to $v = 62$.

2.2 Excited States

In this thesis, only excited states that asymptote to $^1S_0 + ^3P_1$ are considered. For these states, Hund's case c) is the more appropriate choice, where \hat{L} and \hat{S} couple strongly, but \hat{L} does not couple to the inter-nuclear axis [20]. In this limit, Ω , J and J_e form a set of "good" quantum numbers.

States asymptotic to $^1S_0 + ^3P_1$ can have $\Omega = 0, 1$ and either even (g) or odd (u) symmetry. In addition, for $\Omega = 0$ it is usually specified whether the electronic wavefunction is symmetric under reflection at a plane containing the inter-nuclear axis (\pm). Note that this symmetry is different from the \pm symmetry in Hund's case a).

The typical notation for Hund's case c) is $|\Sigma|_{(g/u)}^{\pm}$. The excited states considered in this thesis are $0_u^+(v', J', m'_J)$ and $1_u(v', J', m'_J)$, where v' , J' and m'_J denote the rovibrational structure of the excited state.

2.3 Selection Rules

The most important selection rules for E1 transitions between molecular states are [16]:

$$\begin{aligned} g \leftrightarrow e, g \leftrightarrow g, e \leftrightarrow e \\ \Delta J = 0, \pm 1 \quad (0 \leftrightarrow 0) \\ \Delta v = 0 \quad (\text{for same electronic state}) \end{aligned} \tag{2.3}$$

This thesis describes high precision spectroscopy of the vibrational levels in the ground state potential. According to (2.3), one cannot drive transitions between these levels directly. Therefore, states in the excited potential 0_u^+ will be used as an intermediate state to perform two-photon spectroscopy. The two-photon transition sketched in figure 3.2 thus constitutes the clock transition of the $^{88}\text{Sr}_2$ molecular clock. In addition, resonances in the 1_u potential are used to tune the dynamic polarizability and achieve state insensitive trapping (magic wavelength).

3 Production of Ultracold $^{88}\text{Sr}_2$ Groundstate Molecules

The condition for the molecular clock described in this work is the creation of ultracold molecules that can be probed in a recoil-free way without residual Doppler broadening. Previous work in our group therefore focused on using photoassociation to obtain a tightly confined sample of ultracold molecules from previously laser cooled ^{88}Sr atoms [21].

The experimental apparatus is extensively described in [19].

3.1 Laser Cooling of ^{88}Sr

Our experiments uses the by now standard scheme to cool strontium atoms. Through different cooling stages, it is possible to cool strontium from 800 K to 2 μK within less than 1 s:

1. **Sr oven and Zeeman slower:** A solid block of Sr is heated to ~ 800 K in an oven to produce a hot beam of Sr atoms in the gas phase, collimated by a nozzle with microtubes. A Zeeman slower operates on the strong $^1S_0 \leftrightarrow ^1P_1$ transition (461 nm) [22]. Two repump lasers at 679 nm and 707 nm are used to close the cycle. To drive the transition, an infrared 922 nm external-cavity diode laser (ECDL) is amplified using a tapered amplifier (TA) and frequency doubled through a non-linear crystal in a bow-tie cavity. The laser is locked to the absorption spectroscopy of a Sr vapor cell. The blue light is used for the Zeeman slower, as well as the first magneto-optical trap (MOT) and imaging.
2. **Blue MOT:** The first 3D MOT operates on the strong (32 MHz) blue transition. Due to the strong transition, the capture velocity is high and it is possible to trap $\sim 10^8$ ^{88}Sr atoms at a temperature of ~ 1 mK. The fluorescence of the blue MOT can be easily seen by eye (figure 3.1).
3. **Red MOT:** The second MOT operates on the narrow (7.5 kHz) intercombination line $^1S_0 \leftrightarrow ^3P_1$, which has a wavelength of 689 nm. The narrow line allows cooling

down to $2\ \mu\text{K}$. The red MOT laser is locked to an ultra stable high finesse cavity and has a narrow linewidth of $< 200\ \text{Hz}$ (see section 4.1). We currently trap $\mathcal{O}(10^7)$ atoms in the red MOT.

4. **Optical lattice:** Even at $2\ \mu\text{K}$, the Doppler broadening for $^{88}\text{Sr}_2$ is still $\sim 30\ \text{kHz}$. An optical lattice is a standing wave formed by retro-reflecting an off-resonant dipole trap. The tight confinement along the (in our case 1D) lattice eliminates Doppler shifts due to the now quantized atomic motion. If the trapping frequency is larger than the recoil energy, the recoil due to photon absorption cannot change the motional state of the atom or molecule, enabling so-called recoil-free spectroscopy [23]. The lattice laser is an ECDL at $915\ \text{nm}$, followed by a TA. This system supports a trap depth of $\sim 100\ \mu\text{K}$ and trapping of $\mathcal{O}(10^6)$ atoms.

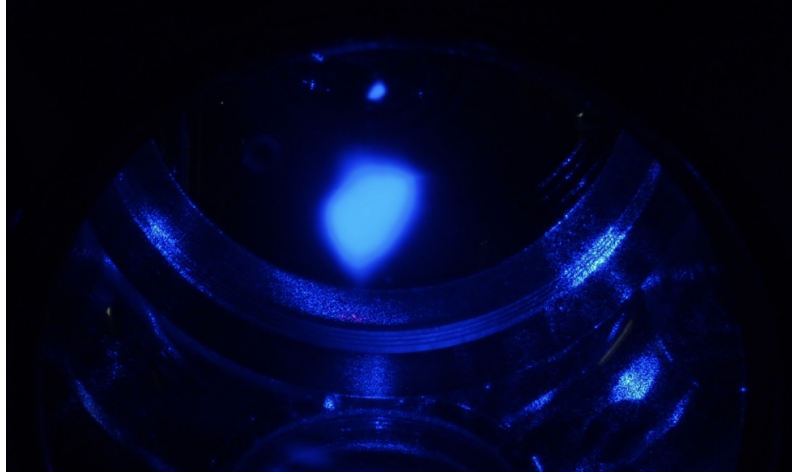


Figure 3.1: Fluorescence of the blue MOT.

3.2 Photoassociation

Photoassociation (PA) is a light-assisted collision, in which two atoms form a weakly bound excited molecule [20]. Here, we use one-photon PA to connect two atoms in the 1S_0 ground state to the $0_u^+(-4, 1)$ molecular state. To obtain ground state molecules, our method relies on the close to unity Franck Condon Factor (FCF) with $X(-1, 0)$: The molecules predominantly decay to a single vibrational level in the ground state potential [21]. To obtain molecules in $X(-2, 0)$, one can use photoassociation via the $0_u^+(-5, 1)$ state instead. This scheme allows the preparation of $\approx 10^4$ in a single quantum state.

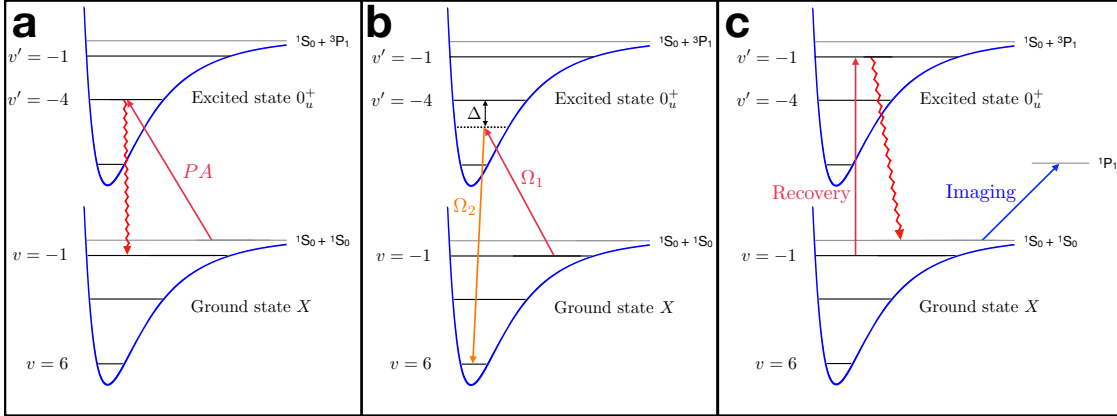


Figure 3.2: Experimental sequence: **a)** PA and predominant decay to $X(-1,0)$. **b)** Raman spectroscopy. **c)** Recovery and imaging of $X(-1,0)$ molecules.

3.3 Imaging

Once $^{88}\text{Sr}_2$ molecules are created, one can perform Raman spectroscopy of deeper lying vibrational levels using two probe lasers. In order to record spectra of the molecule, one has to count the molecules in a specific state.

We typically only count molecules in $X(-1,0)$ and observe the spectra of other states as loss. To image the molecules, they are first turned back into atoms with a short recovery pulse that connects $X(-1,0)$ and $0_u^+(-2,1)$, which efficiently decays to free atoms. These atoms are then imaged using the strong blue transition. The recovery scheme is chosen because the blue transition is almost closed, leading to multiple scattering events per atom and a stronger signal.

The different steps of the experiment are sketched in figure 3.2. The following chapter will describe work on laser stabilization and focus on the specific metrological requirements of a two-photon optical clock.

4 Laser Stabilization

4.1 Clock Laser

The operation of an optical clock consists of repetitively scanning the clock transition while measuring the frequency of the laser. This way, one can lock the laser frequency to the transition, which constitutes the frequency standard. By measuring the laser frequency, it is possible to obtain precise measurements of the energy difference between the clock states. This procedure imposes two requirements onto the clock laser:

1. Short term stability (linewidth): The laser linewidth has to be small enough to resolve the narrow clock resonance and not introduce decoherence during the interaction time (1 ms - 1 s).
2. Long term stability (drift): Since the laser serves as a "flywheel" between interrogation cycles, frequency drifts will corrupt the clock performance.

In order to meet these requirements, one needs a low-drift, narrow frequency discriminator to measure the frequency fluctuations of the laser. It is then possible to feed back on this error signal and thus reduce both linewidth and drift. Fabry-Perot resonators and a laser stabilization using the Pound-Drever-Hall (PDH) technique have become a standard tool in clock-style experiments. The following chapter will summarize the necessary theory of Fabry-Perot resonators and PDH locking. Such a lock is already implemented for the red MOT laser, which is currently the master laser to which the other probe lasers are referenced. In order to improve the two requirements mentioned above, a new clock laser is constructed and its locking performance is analyzed.

In the following discussion, the old clock laser will be abbreviated by A , while the new clock laser will be denoted by α .

4.1.1 Fabry-Perot Resonator

A Fabry-Perot resonator is formed by two opposing spherical mirrors, as depicted in figure 4.1. On resonance, the field interferes constructively with the light that has taken

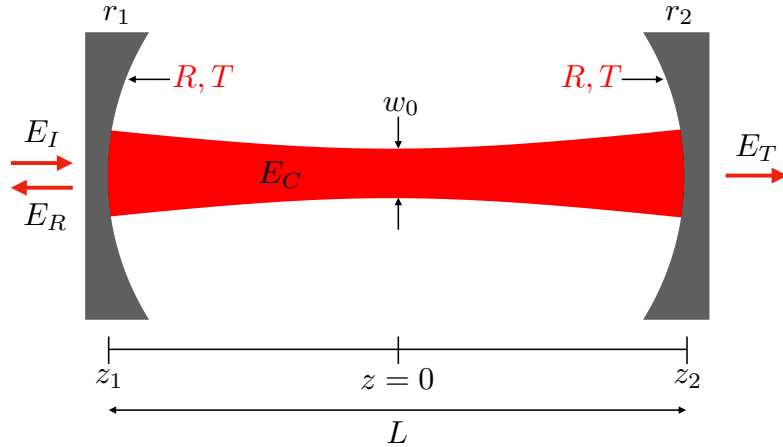


Figure 4.1: Schematic of a Fabry-Perot cavity of length L . R and T are the reflection and transmission coefficients for the intensity. The radii of curvature are denoted by r_1 and r_2 . E_C is the intra-cavity electric field and E_I , E_R and E_T denote the incident, reflected and transmitted field respectively. The red Gaussian beam is a resonant eigenmode of the cavity, with a waist w_0 at position $z = 0$.

an additional round trip, so that the resonance condition can be written as:

$$\phi = m \cdot 2\pi \quad (4.1)$$

where m is an integer and ϕ is the phase picked up by the light during a single round trip. In the geometric optics picture, ϕ would simply be given by $\phi = \frac{2L\omega}{c}$. In contrast, a Gaussian beam picks up an additional phase along its propagation direction, the so called Gouy phase:

$$\xi = -(l + k + 1) \arctan\left(\frac{z}{z_R}\right) \quad (4.2)$$

where z_R is the Rayleigh length of the mode and z the distance from the waist along the optical axis. l and k describe higher order transverse eigenmodes. The fact that the Gouy phase is not the same for all modes lifts the mode degeneracy and therefore different modes can be observed when the laser frequency is scanned. Figure 4.2 shows some of the Laguerre Gauss modes [24], which were observed using a CCD camera behind the cavity while scanning the laser frequency. It is particularly important that the TEM00 mode is not degenerate, since we eventually want to lock the laser to this mode. Because we are mainly interested in the fundamental TEM00 mode, we will drop l and k for the further discussion.

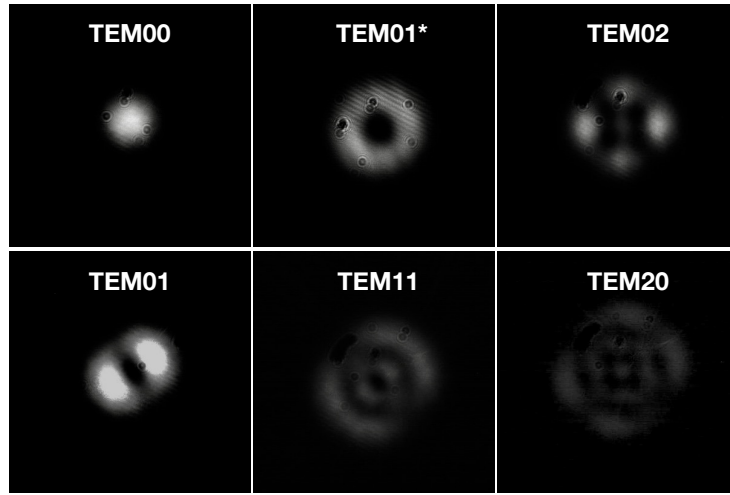


Figure 4.2: Laguerre Gauss modes. Once the cavity is well aligned and mode matched, only the fundamental TEM00 mode persists.

The Gouy phase acquired in one round trip is given by:

$$\xi_{rt} = \arctan\left(\frac{z_1}{z_R}\right) - \arctan\left(\frac{z_2}{z_R}\right) \quad (4.3)$$

Here, z_1 and z_2 are the distances between the two mirror positions and the waist. Finally, we can write the resonance condition as:

$$\phi = \frac{2L\omega}{c} + \xi_{rt} = m \cdot 2\pi \quad (4.4)$$

Knowing the round trip phase shift, we can now calculate the electromagnetic field inside the cavity and its frequency dependence. For an incident laser field E_I , the steady state field inside the cavity E_C fulfills equation 4.5. It is the sum of the transmitted part of the incident field and the intra-cavity field after one round trip.

$$E_C = E_I \sqrt{T} + E_C R e^{i\phi} \quad (4.5)$$

Solving for E_C yields the intra-cavity electric field:

$$E_C = \frac{\sqrt{T}}{1 - e^{i\phi} R} E_I \quad (4.6)$$

Finally, the transmitted and reflected electric field E_T and E_R are related to E_C in a simple way:

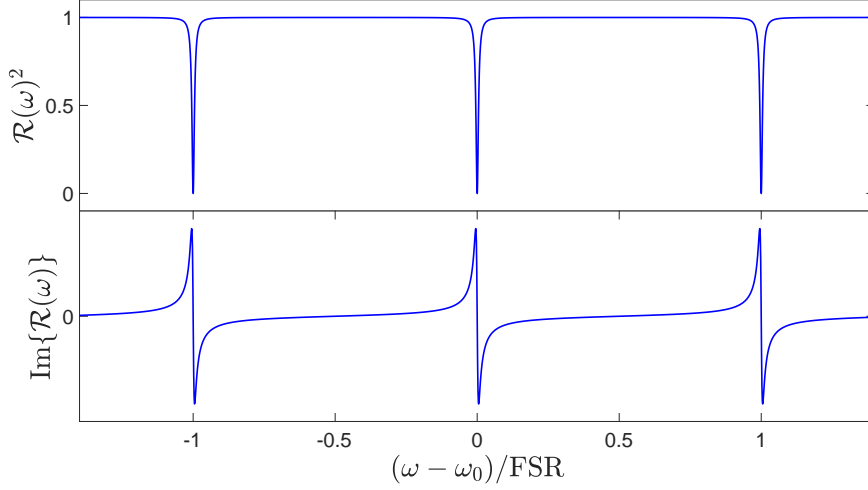


Figure 4.3: Reflection coefficient $\mathcal{R}(\omega)^2$ and its imaginary part. A cavity finesse of 100 is assumed for the plots.

$$E_T = \sqrt{T}e^{i\phi/2}E_C \quad E_R = \sqrt{TR}e^{i\phi}E_C - \sqrt{R}E_I \quad (4.7)$$

Note that the minus sign in E_R arises due to a π phase shift of E_I upon reflection at the backside of the first mirror. For the PDH technique we are mainly interested in the reflected light. The reflection transfer function $\mathcal{R}(\omega)$ becomes:

$$\mathcal{R}(\omega) = \frac{E_R}{E_I} = \sqrt{R} \frac{e^{i\phi} - 1}{1 - Re^{i\phi}} \quad (4.8)$$

The square of the transfer function $\mathcal{R}(\omega)^2$ and its imaginary part are plotted in figure 4.3. The intensity of the reflected light features dips when the resonance condition is met. From equation 4.4 it is clear that the spacing of these resonances is given by the so-called free spectral range (FSR).

$$\text{FSR} = \frac{c}{2L} \quad (4.9)$$

It can be shown that the full width at half maximum (FWHM) of a resonance dip is given by:

$$\text{FWHM} = \text{FSR} \frac{1 - R}{\pi\sqrt{R}} = \frac{\text{FSR}}{\mathcal{F}} \quad (4.10)$$

Free spectral range	FSR	1.5 GHz
Finesse	\mathcal{F}	644 700
Full width at half maximum	FWHM	2.3 kHz
Length	L	10 cm
Radius of curvature 1	r_1	∞
Radius of curvature 2	r_2	50 cm

Table 4.1: Specifications of our commercially available Fabry-Perot cavity by Stable Laser Systems. Note that $r_1 = \infty$ means that the first mirror is flat.

where the finesse \mathcal{F} is a key indicator for resonators and is defined as the ratio between FSR and FWHM of the cavity. The higher the finesse, the narrower the resonance for a given FSR.

$$\mathcal{F} = \frac{\text{FSR}}{\text{FWHM}} = \frac{\pi\sqrt{R}}{1-R} \approx \frac{\pi}{1-R} \quad (4.11)$$

The last approximation is typically made when $\mathcal{F} \gg 100$. Since we want the resonance to be a very narrow frequency discriminator in order to lock the laser, the finesse and thus the mirror reflectivity R are very high for our cavity. Table 4.1 shows some important quantities for our cavity that was bought from Stable Laser Systems (SLS).

SLS initially estimated the finesse to be 478 000 by measuring the mirror reflectivities. This approach has a relatively large error and also depends on a somewhat rough estimate of the mirror losses. To get an independent measurement, one could simply measure the FWHM of a resonance. However, since the resonance is so narrow, this would require a laser which is already narrower than the resonance.
An alternative approach is to measure the energy decay inside the cavity once the laser field is shut off. The energy decay rate is proportional to the energy stored inside the cavity, where the proportionality constant is determined by the mirror's reflectivities (for a loss-less cavity).

$$\frac{dE}{dt} = -\frac{E}{\tau} \quad (4.12)$$

This equation is solved by an exponential, where the decay constant τ is the photon lifetime inside the cavity.

$$E(t) = E_0 e^{-t/\tau} \quad (4.13)$$

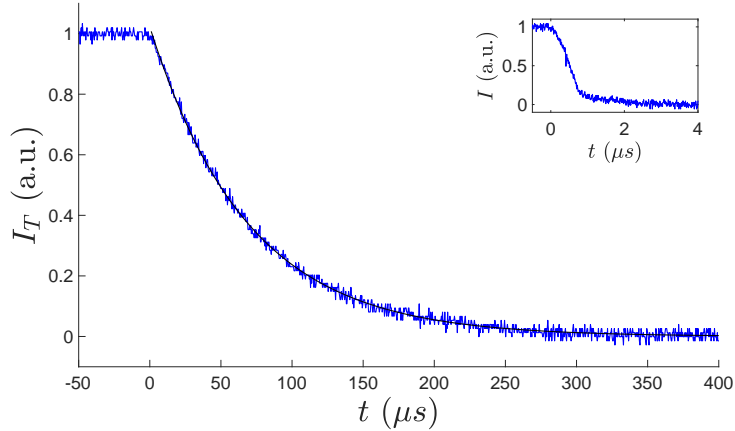


Figure 4.4: Intensity decay of the transmitted light. The laser was quickly shut off at $t = 0$ using an AOM. The inset shows the combined response time of RF, AOM and the photodiode, which was determined to be $\sim 1 \mu\text{s}$. The decay constant from an exponential fit is $\tau = 68.5(5) \mu\text{s}$, corresponding to a finesse of $\mathcal{F} = 644700(500)$.

The energy decays by $1 - R$ in a time L/c , such that τ is given by:

$$\tau = \frac{L}{(1 - R)c} = \frac{\mathcal{F}L}{\pi c} \quad (4.14)$$

We can measure the decay time by stabilizing a laser to a cavity resonance and then quickly switching off the light while recording the transmitted light on a fast photodiode. To quickly extinguish the laser, we use an acousto-optical modulator (AOM) [25]. The first order of the AOM is stabilized on the cavity resonance and the AOM's radio frequency (RF) signal is switched off using a TTL RF switch. The combined response time of the RF, AOM and photodiode is shown in the inset in figure 4.4 and is on the order of $1 \mu\text{s}$, i.e. much faster than the cavity decay.

From the measurement depicted in figure 4.4 we obtain a finesse of $\mathcal{F} = 644700(500)$ using equation 4.14, which is substantially larger than the value estimated by SLS. This translates to a resonance width of FWHM = 2.3 kHz, which gives us a very narrow frequency discriminator that we can use to obtain an error signal for the laser.

In order to lock the laser to a cavity resonance, we need an error signal that changes sign at the center of the resonance so that the lock can correct the frequency with the right sign. The imaginary part of the transfer function in figure 4.3 carries information about the phase of the reflected light and features exactly that quality. The idea behind the PDH technique is to access this phase information to obtain a narrow error signal.

4.1.2 PDH Locking

This section gives a summary of our implementation of PDH locking to a high finesse cavity. Useful reviews of the PDH technique are given in [26, 27].

In order to see how the PDH error signal measures $\text{Im}\{\mathcal{R}(\omega)\}$, let's consider a phase modulation of the laser beam incident on the cavity and its effect on the reflected field.

$$E_I = E_0 e^{i[\omega t + \beta \sin(\Omega t)]} \quad (4.15)$$

Here, β and Ω are the modulation index and frequency respectively. We can approximate equation 4.15 using the Jacobi-Anger expansion, keeping only the first two terms, where J_0 and J_1 are Bessel functions of the first kind. Finally, the terms are rewritten in the last equation to see how side bands appear in frequency space:

$$E_I \approx E_0 [J_0(\beta) + 2iJ_1(\beta)\sin(\Omega t)] e^{i\omega t} = E_0 [J_0 e^{i\omega t} + J_1(\beta) e^{i(\omega+\Omega)t} - J_1(\beta) e^{i(\omega-\Omega)t}] \quad (4.16)$$

We can now use the transfer function from equation 4.8 to obtain the reflected field: $E_R = \mathcal{R}E_I$. As the photo detector measures intensity and not electric field, we compute the intensity of the reflected light:

$$I_R = \frac{1}{2} [\mathcal{R}(\omega)E_c + \mathcal{R}(\omega + \Omega)E_s e^{i\Omega t} + \mathcal{R}(\omega - \Omega)E_s e^{-i\Omega t}]^2 \quad (4.17)$$

Where the indices c and s have been introduced for the reflected field of the carrier and side bands respectively. After some algebra and taking the approximation $\Omega \gg \text{FWHM}$ we find:

$$\begin{aligned} I_R = & I_c \mathcal{R}(\omega)^2 + I_s [\mathcal{R}(\omega + \Omega)^2 + \mathcal{R}(\omega - \Omega)^2] \\ & + 2\sqrt{I_c I_s} \left[\text{Im}\{\mathcal{R}(\omega)\mathcal{R}^*(\omega + \Omega) - \mathcal{R}^*(\omega)\mathcal{R}(\omega - \Omega)\} \right] \sin(\Omega t) \\ & + \text{terms} \propto \sin(2\Omega t) \end{aligned} \quad (4.18)$$

Since we are interested in $\text{Im}\{\mathcal{R}\}$, we introduce a band pass filter centered around Ω to isolate the term in the second line. The filtered signal is now proportional to the PDH error signal $\epsilon(\omega)$, oscillating at the modulation frequency Ω . Lastly, the photo diode signal gets mixed down with a reference signal with frequency Ω to obtain the DC error signal $\epsilon(\omega)$.¹

¹Note that the photodiode signal has to be mixed with a reference with the right phase. In order to control this relative phase, a delay box is introduced in the reference signal path.

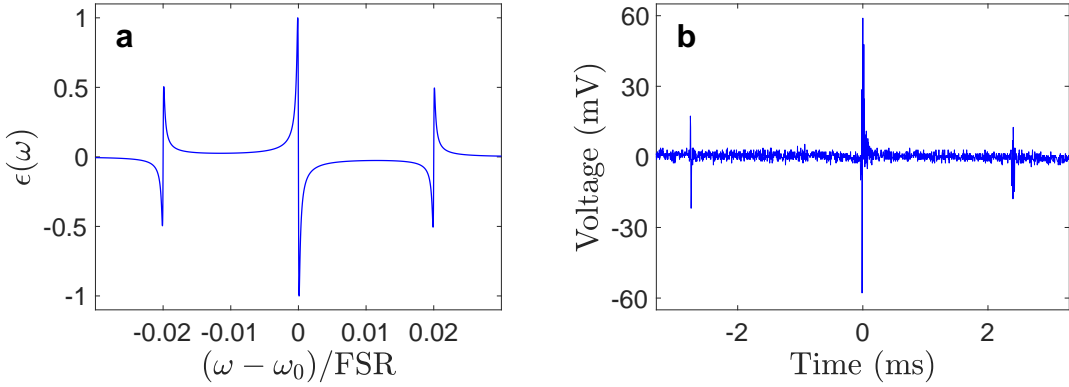


Figure 4.5: **a)** PDH error signal for $\Omega = 0.02 \cdot \text{FSR}$, $\mathcal{F} = 5000$. **b)** Measured error signal for the $\mathcal{F} = 644\,700$ cavity. Since the unlocked laser linewidth is much larger than FWHM, this signal looks very different from sweep to sweep.

$$I_{\text{filter}} = \epsilon(\omega) \sin(\Omega t) \\ \epsilon(\omega) = 2\sqrt{I_c I_s} \left[\text{Im}\{\mathcal{R}(\omega)\mathcal{R}^*(\omega + \Omega) - \mathcal{R}^*(\omega)\mathcal{R}(\omega - \Omega)\} \right] \quad (4.19)$$

Figure 4.5 is a plot of $\epsilon(\omega)$ and we immediately recognize the similarity to $\text{Im}\{\mathcal{R}(\omega)\}$ plotted in figure 4.3. On resonance, the carrier experiences a frequency-dependent phase shift and interferes with the side bands, which are entirely reflected (since $\Omega \gg \text{FWHM}$). This interference exhibits a beating pattern and thus oscillates at Ω . By measuring this beat note, the PDH technique allows us to access the phase of the reflected light, which is now encoded in a signal oscillating at frequency Ω . Since Ω is much smaller than the light frequency ω , it is now possible to measure the cavity response on a photo detector.

4.1.3 Setup and Locking Procedure

The narrow error signal derived above allows one to reduce the linewidth of a laser significantly by locking it to a cavity resonance. Initially, we bought a commercial ECDL by Sacher Lasertechnik, which turned out to have severe issues with internal ground loops introducing 60 Hz noise to the laser. Since Sacher was not able to fix the problem, we decided to construct a new ECDL instead, based on a design by our Postdoc Stanimir Kondov, which turned out to work very well for our application. Details regarding the design of the ECDL can be found in appendix A.1.

In order to reach high finesse and a laser lock limited by the thermal noise floor of

the cavity, the resonator has to be in vacuum (1×10^{-7} torr). The cavity was bought in combination with a vacuum housing, ion pump and temperature control from SLS. Since it was already set up when I joined the lab, the setup will not be discussed in this thesis and it is referred to SLS for further information [28].²

Mode Matching

To maximize the coupling efficiency, the Gaussian mode of the laser has to match the fundamental mode of the cavity, since the coupling efficiency is proportional to the overlap integral between laser field and cavity mode field [29]. In order to match the modes, one first has to calculate the size and location of the cavity mode waist. The radius of curvature $R(z)$ of an eigenmode matches the radii of curvature r_1 and r_2 at the two mirrors. In this way, the waist will occur at the same position after a round trip, corresponding to a stable mode. Since the first mirror of our cavity is flat, the waist is located at the first mirror ($z = 0$). It is then easy to calculate the mode waist ω_0 and the mode Rayleigh range z_R using Gaussian beam optics [24]:

$$R(L) = L \left[1 + \left(\frac{z_R}{L} \right)^2 \right] = r_2 \quad (4.20)$$

$$z_R = L \sqrt{\frac{r_2}{L} - 1} = 0.2 \text{ m} \quad (4.21)$$

$$\omega_0 = \sqrt{\frac{\lambda z_R}{\pi}} = 223 \mu\text{m} \quad (4.22)$$

To match the beam, the waist is measured at the EOM position with a camera. A Matlab script then iteratively shifts lenses f_2 and f_3 and calculates the new waist and its position. The program finds several solutions that lead to mode matching, giving a good starting point for the lens placement. Once the lenses are placed at the calculated position, a camera is placed at the same distance from the PBS as the first cavity mirror. Slight adjustments of f_2 and f_3 are made to focus on the camera with the desired waist.³

Alignment

To align the cavity, it is useful to install a camera at the back of the cavity to identify different modes. The following steps are taken:

²Our model features a notched cavity design and an ultra low expansion glass (ULE) spacer defines the distance between the two mirrors.

³Note that equation 4.22 describes the waist of the electric field. The camera measures the waist of the intensity, and thus $2\omega_0$.

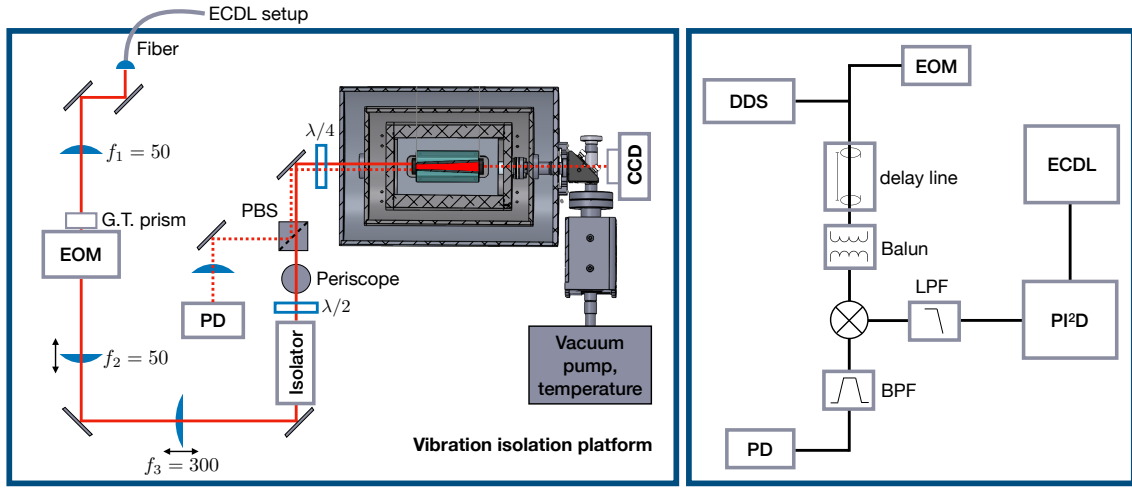


Figure 4.6: Optics setup for PDH locking and schematic of the electronics used to extract the error signal.

1. Looking through the back window of the cavity, one can observe a concentric aperture indicating the mirror edges. With the help of a second person, one can align an iris with its center matching the center of the mirror.
2. The iris is almost closed and the laser is aligned to the iris using the penultimate mirror.
3. The last mirror is adjusted to overlap the reflected light with the incoming beam. Iterate steps 2 and 3 until both are satisfied.
4. Now the laser frequency should be scanned slowly ($\sim 1 \text{ Hz}$) while looking at the camera. Usually, higher modes are observed first. The lowest observed mode should be maximized. This usually makes even lower modes visible. Reiterate until the TEM00 mode is observed and maximize it.
5. At this point, one can look at the photodiode signal and increase the signal height of the TEM00 mode by walking the last two mirrors.
6. Once the signal is high enough to lock the cavity, one should optimize the transmitted power while the laser is locked. The mode matching can be optimized by adjusting the lenses.
7. If the alignment is satisfactory, one can put two irises in the beam path and thus "save" the alignment, since two fix points completely define the beam alignment.

If a component is bumped or has to be changed, one can simply align the beam to the irises and get a good enough alignment to quickly restore the lock.

The alignment of the cavity is quite sensitive and it can be difficult to align it from scratch. This is due to the fact that the unlocked laser has a linewidth of ~ 500 kHz, i.e. much larger than the cavity linewidth of 2.3 kHz. Therefore, we use a different wavelength (650 nm) for which the finesse is much lower for pre-alignment. Once the TEM00 is observed, we switch to the 780 nm laser and can start the fine alignment at step 4.

The laser light is guided to a vibration isolated platform (Minus K, Model 250BM-1) through a polarization maintaining single mode fiber. An electro-optical modulator (EOM) is driven by a direct digital synthesizer (DDS) and modulates the laser phase. Since the aperture of the EOM is too small for the laser beam, a 1 : 1 telescope is used to focus the beam onto the EOM. The second mirror of the telescope and a third lens are used for mode matching to the cavity and are therefore mounted onto an adjustable cage.

To detect the reflected light, one uses a polarizing beam splitter (PBS) and a $\lambda/4$ wave plate. The reflected light passes the wave plate twice and thus has a polarization orthogonal to the incoming beam. It is picked up using the PBS and focused onto a photodiode. The output of the photodiode is then bandpassed and mixed down using the same DDS signal that also drives the EOM. In addition, a balun is introduced to break possible ground loops.

Residual Amplitude Modulation

One major source for locking errors in the PDH scheme is residual amplitude modulation (RAM). Although the photodiode is band pass filtered at the modulation frequency, there are RAM effects that can be demodulated with the locking signal and thus perturb the DC error signal, leading to locking errors.

Two flat surfaces along the optical path can introduce an etalon. The resulting interference changes the DC offset of the error signal and is highly temperature dependent. A good strategy is to slightly tilt all optical elements. In our case it turned out to be difficult to completely eliminate an etalon formed by the EOM crystal and the cavity incoupling mirror. Since the focus is at the EOM position, the flat wave front favors etaloning. To fully eliminate the etalon, an optical isolator can be introduced in the etalon path.

Another important RAM effect can be induced by the EOM. For a polarization deviating from the z-cut axis of the EOM, the light will exhibit RAM, reaching a maximum for

45° polarization relative to the z-cut axis [30]. In order to minimize this effect, a Glan Thompson polarizer with extinction ratio of 1 : 10 000 is used. It should be noted that the higher than expected finesse of our cavity actually helps to diminish RAM effects, since changes in the DC offset lead to a smaller locking error for smaller cavity linewidths. To further eliminate RAM, it is also possible to servo on the EOM voltage to align the principal axes of the crystal to the polarization [30].

Locking Procedure

In order to lock the laser, we use a Vescent D2-125 laser servo. In its simplest form, a servo relates input and output by a transfer function $G(\omega)$ which is frequency dependent. The D2-125 has proportional, dual integral and differential gain (PI^2D) and the different gain corners can be individually adjusted [31]. The gains and servo settings are adjusted to optimize the transfer function and obtain a stable lock and good noise suppression (see figure 4.7).

Since the laser linewidth is so much larger than the cavity linewidth it can be very hard for the servo to catch the lock. A useful trick turned out to work very well and makes locking quite easy. One simply brings the laser somewhat close to resonance and then turns on the lock. Most likely the laser will not lock, but rather rail to the maximum servo output immediately. The DC offset is then turned until the servo rails in the opposite direction. The laser is therefore swept across the resonance and catches lock. Then the DC error is brought back to zero again to lock the laser exactly on resonance.

4.1.4 Evaluation of the Locking Performance

In order to evaluate the locking performance, one can analyze the spectrum of the error signal while the laser is locked to the cavity. This measurement is shown in figure 4.7 and reveals a servo bandwidth of ~ 800 kHz. The servo parameters have been tuned to maximize the servo bandwidth and maintain good noise suppression across the whole servo bandwidth. The lock is very robust against acoustic noise (talking, clapping, music, etc.) and has been locked for ~ 20 h. Hitting the laser table with a metal object like a screwdriver usually unlocks the laser, which couldn't be overcome by optimizing the lock settings.

Evaluating the error signal gives us the servo bandwidth, but it can't be used to obtain a reliable measure of the laser linewidth. The optimal method to measure the laser linewidth γ is self-heterodyne beating [32]. One part of the laser is sent through a long delay fiber and shifted by an AOM before being recombined with the non-delayed part on a beam splitter. This interference creates a beat note at the AOM frequency. If the

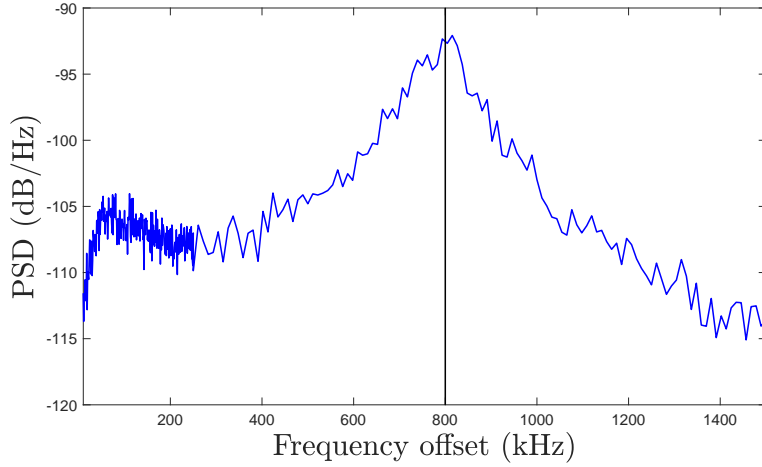


Figure 4.7: Power Spectral Density (PSD) of the error signal while the laser is locked. The black line indicates the servo bandwidth. For frequencies below 250 kHz, a smaller resolution bandwidth was used.

length of the delay fiber is larger than the coherence length of the laser, the two parts can be treated as independent lasers with the same linewidth. The resulting beat note is given by the convolution of the two linewidths and has a width of 2γ . This approach is not feasible for a very narrow laser, since the coherence length for a 1 Hz wide laser is roughly 1×10^8 m, which is about a quarter of the distance from the Earth to the Moon.

Another possibility is to use two independent lasers and beat them against each other, resulting in a beat note width of $\gamma_{\text{beat}} = \gamma_1 + \gamma_2$. We have another relatively narrow laser in the lab, which is also locked to a high finesse cavity ($\mathcal{F} \sim 30\,000$) and is used for our red MOT at $\lambda_A = 689$ nm. Unfortunately, the resulting beat note frequency with the $\lambda_\alpha = 780$ nm laser is too high to be detectable. However, we can use a frequency comb to bridge this gap and indirectly compare the two lasers. To do that, the comb is locked to λ_A and the beat note between comb and λ_α is measured. Details of how the comb lock is achieved can be found in section 4.3.

The resulting beat note is shown in figure 4.8 and has a width of ~ 200 Hz. A range of 5 kHz is swept with a resolution bandwidth of 10 Hz and averaged over 10 sweeps. The total duration of the measurement is ~ 10 s, which corresponds to the typical time it takes to scan a molecular transition in our experiment.

Since the finesse of the A laser cavity is a lot smaller than for the new α clock laser, this width is likely dominated by A . The smallest linewidth observed for a single photon transition with A laser was 150 Hz, but it was not entirely clear if the width is laser

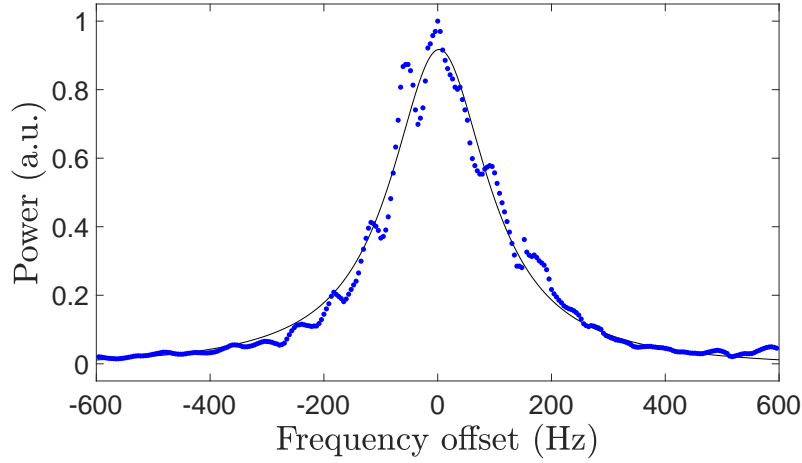


Figure 4.8: Beat note of α laser with a frequency comb, which is locked to A laser. The width of the fitted Lorentzian is 208 Hz

limited. Although this result only gives a stringent upper bound of $\gamma_\alpha = 200$ Hz, the actual width is more likely on the order of 10 Hz or lower, which is achieved by other groups with a similar setup [33, 34].

Moreover, one can measure the frequency drift of the cavity using the frequency comb. To do that, the comb is locked to α and the repetition rate is counted for ~ 3 h (see section 4.3). A linear fit yields $\frac{df_\alpha}{dt} = 390 \text{ mHz/s} = 33.7 \text{ kHz/d}$. This is slightly larger than the 20 kHz/d specified by SLS. SLS measured the zero-crossing temperature of the cavity spacer to be 50.8 °C using a speed of sound measurement. The cavity drift could potentially be minimized by measuring the zero crossing more carefully using the frequency comb.

4.2 Fiber Noise Cancellation and Intensity Stabilization

Once a narrow linewidth is achieved, the light has to be distributed across the experiment to perform spectroscopy or metrology using the frequency comb. Since our experiment consists of multiple optical tables, we use optical single mode fibers to distribute the light. In order to preserve the polarization on passage through the fiber, we use polarization maintaining (PM) fibers.

In this section we study the effects of single mode fibers on the spectral purity of the light. A simple test of the fiber induced phase noise is the self heterodyne measurement discussed in 4.1.4. Since the fiber is much shorter than the coherence length of the laser, one would essentially expect a zero width for the beat note, since the laser is coherently compared to itself. Any finite width can therefore be attributed to phase noise induced in the fiber through acoustic fluctuations.

Acoustic noise in the lab environment changes the refractive index n of the fiber locally, leading to a time dependence of the optical path length OPL and therefore the laser phase ϕ :

$$OPL(t) = \int_{\text{fiber}} n(z, t) dz \quad (4.23)$$

$$\phi(t) = \omega t + \frac{2\pi \cdot OPL(t)}{\lambda} \quad (4.24)$$

In order to cancel this phase noise, we use a modified version of the fiber noise cancellation (FNC) technique first described in [35]. In addition, our setup includes intensity stabilization of the fiber output. Both fibers carrying the Raman lasers feature FNC and intensity stabilization. In addition, the fiber connecting the old clock laser A and the frequency comb is fiber noise canceled.

4.2.1 Setup

The setup in figure 4.9 is capable of both fiber noise cancellation as well as intensity stabilization.

The first order of an AOM, driven by a voltage controlled oscillator (VCO) at $f_{\text{AOM}} = 80 \text{ MHz}$, is coupled to a PM single mode fiber (black arrows). About 10 % of the light gets reflected at a partially reflecting mirror and travels back through the fiber (red dashed arrows). Its 0th order then overlaps with a reference beam (black dashed arrows). The reference beam passes the AOM in 0th order, gets fully reflected and passes the AOM again, this time in the -1st order. The two beams are therefore shifted against

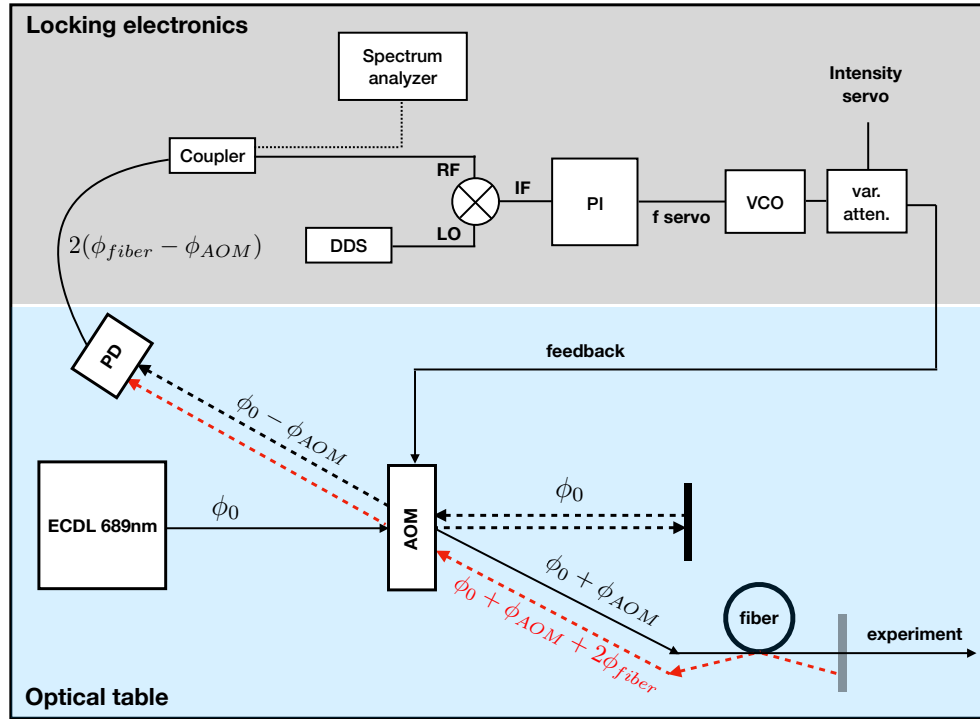


Figure 4.9: Setup for FNC and intensity stabilization.

each other by $2f_{AOM}$. The reference beam is independent of any fiber noise, whereas the probe beam has passed the fiber twice.

The fibers are all shorter than 20 m, corresponding to a fiber passage time of ~ 100 ns. This is much shorter than the typical timescale of acoustic noise (< 20 kHz corresponds to > 50 μ s). Therefore, we assume that the optical path length is the same for both passes. The width of the beat note between probe and reference is then given by twice the fiber noise spectrum induced in the optical fiber.

Without FNC, the fiber noise can lead to spectral broadening on the order of 100 Hz and is highly dependent on the acoustic environment. Furthermore, small details in the handling of the fibers and how the fibers are fastened can significantly change the noise behavior.

The beat note is detected using a fast photodiode (bandwidth 1.2 GHz) and mixed with a DDS signal at $2f_{AOM}$ to produce a DC error signal for the lock. This error signal is then fed into an analog PI controller.⁴ The output of the servo is added onto a DC set point and is applied to the V_{tune} input of the VCO.

⁴Designed by Stanimir Kondov, adapted by Kon Leung.

In order to integrate intensity stabilization into the same setup, the VCO output is followed by a voltage controlled variable attenuator. The fiber output power is monitored by branching off a small portion of the light using a beam sampler and detected with a photodiode. To lock the intensity, we use a commercial servo box (Newport, Model LB1005-S).

4.2.2 Evaluation of Cancellation Performance

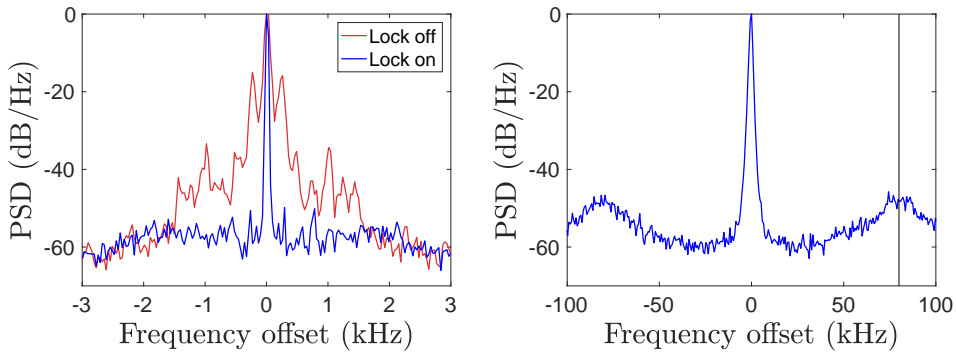


Figure 4.10: PSD of the out of loop beat note for FNC and the unlocked system. The left figure is a high resolution scan of the peak. The servo bandwidth is ~ 80 kHz, as indicated by the black line.

To evaluate the locking performance, we could simply use the in-loop photodiode signal. However, a much cleaner test consists of directly comparing the light before and after the fiber with an additional detector.

To do this, the fiber is simply wound in a circle and the output is recombined with the light before the fiber on a beam splitter. This way, only a single fiber pass is probed and the resulting beat note has a width determined exactly by the noise introduced in the fiber.

Figure 4.10 shows the beat note for both the unlocked and locked system. For tests of the unlocked system we use a DDS to drive the AOM, since the unlocked VCO output has a width of several kHz. The PSD clearly shows a great reduction of the noise in the kHz range and exhibits a servo bandwidth of 80 kHz. The central peak of the locked system is limited by the resolution bandwidth of the spectrum analyzer (10 Hz).

To see how good the noise suppression works for a particular frequency, one can induce excess acoustic noise on purpose and measure the response of the lock. To do that, a simple sine tone is played on a speaker placed near the optical table. A sound pressure level of 80 dB corresponds to a modulation depth of $\beta \sim 0.2$ and the response function of

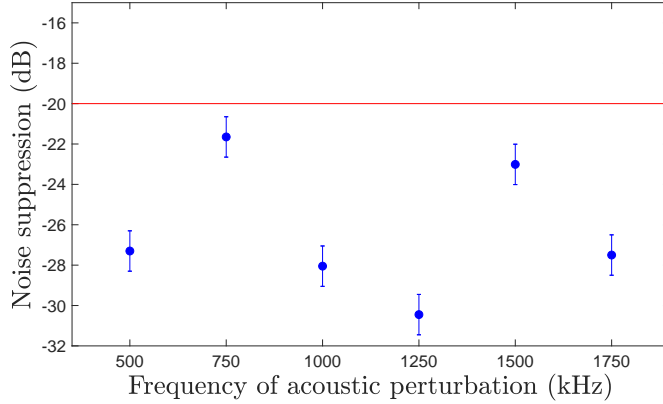


Figure 4.11: Side band suppression for a 80 dB acoustic perturbation.

the fiber is relatively flat between 200-2000 Hz. The sine tone modulates the refractive index in the fiber and thus leads to phase modulation according to equation 4.23. As already discussed in section 4.1.2, this imposes side bands onto the laser spectrum. The side band power is measured relative to the carrier in dB c. The noise suppression is then defined as the ratio between side band powers for the locked and unlocked system. Figure 4.11 shows that the suppression is better than -20 dB between 500-1750 Hz, an important range for many everyday acoustic noise sources.

To get an even better estimate of how stable the transfer through the fiber is, we use a frequency counter to obtain a time series of frequencies f_i for the beat note. The standard way to analyze the stability in the temporal domain is to compute the so called Allan deviation [36, 37].

Compared to the standard deviation, the Allan deviation σ_y has the advantage of converging for most types of power-law oscillator noise. It computes the difference between successive measurements for different gate times, where overlapping samples can be used to improve the statistics. The Allan deviation is defined as follows:

$$\sigma_y = \frac{1}{2} \langle (y_{i+1} - y_i)^2 \rangle \quad (4.25)$$

$$y_i = \frac{f_{i+1} - f_i}{\tau} \quad (4.26)$$

where $\langle \rangle$ denotes the mean value. The beat note was continuously measured over 12 h with a gate time of 1 s. Figure 4.12 shows the Allan deviation, calculated for the fractional stability of the laser $\frac{f_i - \langle f_i \rangle}{f_{\text{Laser}}}$.

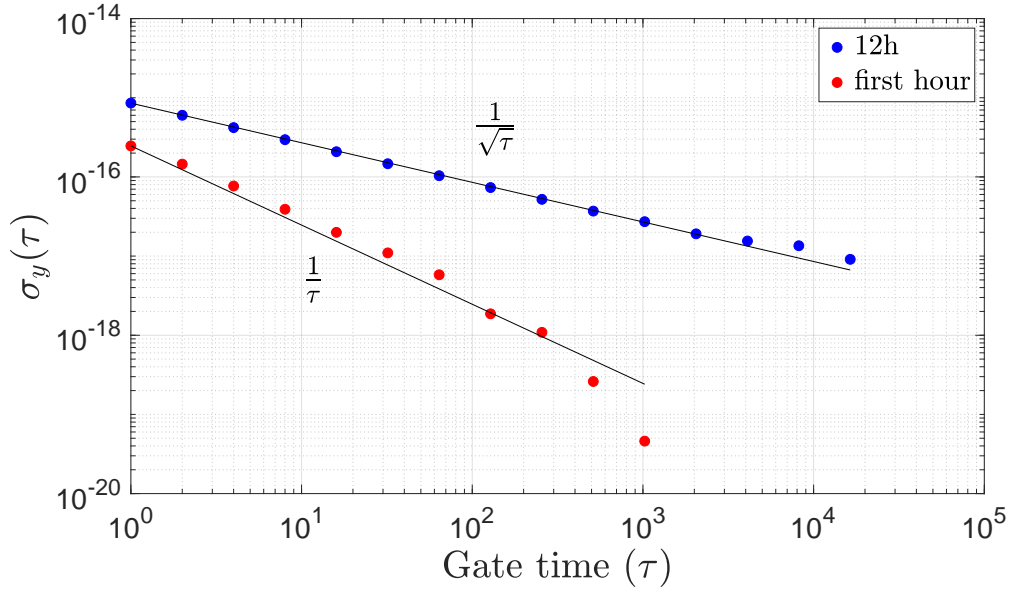


Figure 4.12: Allan deviation of the fractional instability between two remote locations with FNC. $\frac{1}{\tau}$ and $\frac{1}{\sqrt{\tau}}$ slopes are drawn to guide the eye.

Inspection of the time series reveals that 11 cycle slips occurred during the measurement, where we have defined a cycle slip as a deviation from the mean by more than 10σ . It is not quite clear if the cycle slips stem from the lock or simply constitute an error of the counter, since a very high signal to noise ratio is necessary for reliable counting. No cycle slips occurred during the first hour of the experiment and the Allan deviation for this sub-sample is plotted in red for comparison. The full data set averages down as $\frac{1}{\sqrt{\tau}}$, whereas the cycle slip free subset averages as $\frac{1}{\tau}$, which would be expected for a white phase noise spectrum. It seems likely that the $\frac{1}{\sqrt{\tau}}$ dependence is an artifact of the cycle slips. In any case, the Allan deviation is more than good enough for our purposes. We estimate the Allan deviation of our new clock laser to be $\sim 2 \times 10^{-15}$ at 1 s, based on information by SLS and the results of several other groups [33, 34]. For the full data set, the Allan deviation averages down to 9×10^{-18} and reaches even 5×10^{-20} for the cycle slip-free first hour of the measurement.

To find out if the cycle slips are actual slips in the lock or counting errors, one could record the servo output and look for correlations between cycle slips and servo output spikes. If the slips actually correspond to locking errors, one could possibly improve the system by using a tracking VCO if even higher stability is desired [38].

4.3 Stability Transfer Using a Frequency Comb

The development of femtosecond frequency combs has revolutionized the field of optical frequency metrology by linking radio frequency standards to the optical domain. Prominently, it has opened the possibility for optical clocks. Consequently, John L. Hall and Theodor W. Hänsch were awarded the Nobel Prize in Physics 2005 for its development [39, 40]. This section gives a short review of frequency combs and concentrates on the applications of stability transfer and frequency metrology. An in-depth review can be found in [41].

4.3.1 Elastic Tape Model

Our lab has bought a commercial frequency comb by Menlo Systems (Model FC1500). It is based on a mode locked fs fiber laser. The output consists of a series of pulses separated by the cavity round trip time T . The Fourier transform of such a pulse train is given by a series (comb) of narrow modes, separated by the pulse repetition rate f_{RR} . The electric field can thus be described as a carrier wave oscillating at ω_c , multiplied by an envelope with periodicity T (see figure 4.13).

$$E(t) = \text{Re} \left\{ A(t) \cdot \exp(-i\omega_c t) \right\} = \text{Re} \left\{ \sum_n A_n \cdot \exp[-i(\omega_c + n\omega_{RR})] \right\} \quad (4.27)$$

Where A_n are the Fourier components of the periodic envelope function $A(t)$. As the carrier wave moves at a phase velocity different from the envelope's group velocity, the carrier acquires a phase shift relative to the envelope for each pulse. This phase advance $\Delta\phi_{CEO}$ per pulse is called carrier envelope offset (CEO) and translates to a frequency offset in the spectral domain:

$$f_{CEO} = \frac{1}{2\pi} f_{RR} \Delta\phi_{CEO} \quad (4.28)$$

The comb spectrum is thus described by the so called elastic tape model, where the comb tooth number n labels the different modes and is typically chosen so that $f_{CEO} < f_{RR}$.

$$f_n = f_{CEO} + n f_{RR} \quad (4.29)$$

If both f_{CEO} and f_{RR} can be locked to a stable reference, the frequency comb can act as an "optical ruler". One can simply compare a laser with unknown frequency to a comb tooth m . If m , f_{CEO} , f_{RR} and the beat note are known, one can obtain the absolute frequency of the laser.

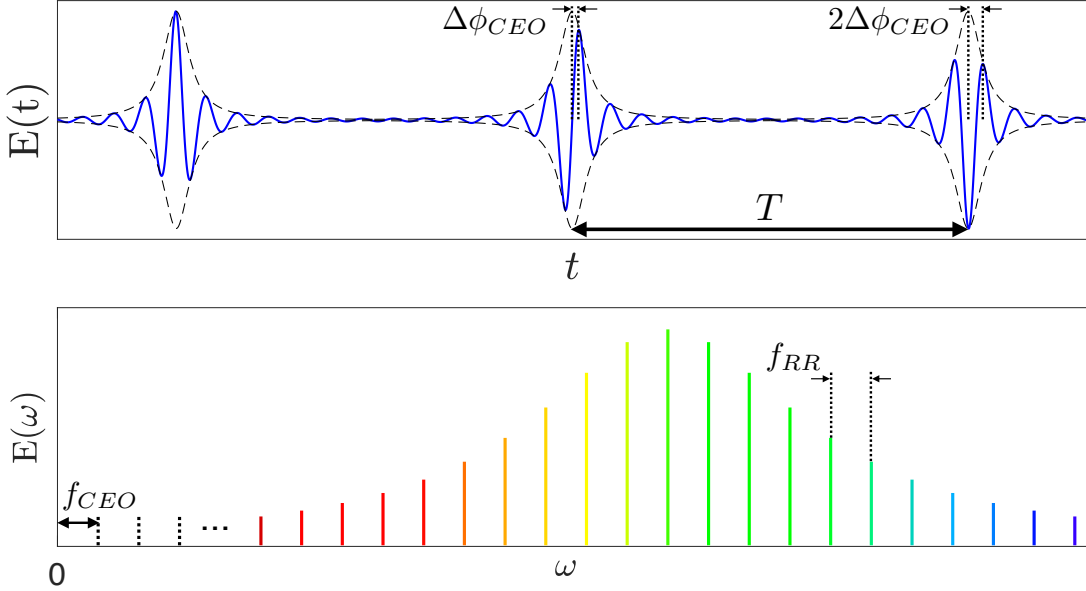


Figure 4.13: Frequency comb in the temporal (top) and frequency (bottom) domain (not to scale).

The benefit of this scheme is that it only requires measurements in the RF domain, but gives access to measurements of optical frequencies. In the Menlo comb, f_{RR} is directly measured and f_{CEO} is obtained via a so called f-2f interferometer: When the comb light is frequency doubled (SHG), f_{CEO} is doubled, whereas f_{RR} stays the same. This is due to the fact that frequency summation is the dominant effect in SHG [42]. If the comb is now frequency doubled and compared to the original mode $2n$, the beat note δ is given by f_{CEO} .

$$\delta = 2f_{CEO} + 2nf_{RR} - (f_{CEO} + 2nf_{RR}) = f_{CEO} \quad (4.30)$$

In order for this scheme to work, it is necessary that the comb spans an entire octave. Therefore, a photonic crystal fiber (PCF) is used to generate a broad super continuum (SC), based on self-phase modulation, which largely preserves the coherent properties of the light [43, 44]. Finally, since we are interested in the comb spectrum between 650 nm and 925 nm, the comb output is followed by a SHG unit and a PCF, generating a broad comb spectrum in the visible range.

4.3.2 Stability Transfer

Since the clock transitions that we want to probe are two-photon transitions, the relevant measure for metrological capability is the relative fractional stability between the two

Raman lasers. Ideally, one would therefore phase lock the two and obtain essentially perfect relative phase coherence. However, there are no suitable detectors for transition energies on the order of 20 THz, which makes it impossible to detect a beat note between the two lasers. Instead, we use the frequency comb to transfer stability from a stable clock laser (master) to the second laser (slave). It has been shown that in principle this scheme can be used to transfer stability on the order of 10^{-18} [45].

For current experiments, we use the old clock laser A at 689 nm as a master, which has a linewidth of < 200 Hz and a slave laser at 651 nm. The idea is to lock f_{RR} to the master and then lock the slave to the frequency comb while f_{CEO} is locked to an RF reference.⁵ To analyze how this works, let's first consider the beat note between master and comb:⁶

$$\delta_{MC} = 2f_{CEO} + n_M f_{RR} - f_M = \text{const.} = 0 \quad (4.31)$$

This beat note is used to lock f_{RR} through feedback on a cavity piezo element and an intra-cavity EOM, allowing for high enough bandwidth to obtain a proper phase lock. This lock "fixes" the beat note δ_{MC} to a constant that we choose to be zero for convenience. The beat note with the slave will then be given by:

$$\begin{aligned} \delta_{SC} &= 2f_{CEO} + n_S f_{RR} - f_M \\ &= 2f_{CEO} \left(1 - \frac{n_S}{n_M}\right) + \frac{n_S}{n_M} f_M - f_S = \text{const.} = 0 \end{aligned} \quad (4.32)$$

where we have substituted f_{RR} from equation 4.31.

This beat note is fixed to a constant again through a phase lock, this time through feedback on the current and piezo of the slave laser. If we solve equation 4.32 for f_S , we see that f_S is now proportional to f_M .

$$f_S = 2f_{CEO}\beta + \frac{n_S}{n_M} f_M \quad (4.33)$$

where we have introduced the important factor $\beta = 1 - \frac{n_S}{n_M}$.

If f_{CEO} and f_M have a stability (linewidth) of Δf_{CEO} and Δf_M respectively, the slave laser will inherit the following stability (if we assume the uncertainty introduced by f_{RR} to be small):

$$\Delta f_S = 2\beta\Delta f_{CEO} + \frac{n_S}{n_M}\Delta f_M \quad (4.34)$$

⁵Note that all RF sources used in the locking of the comb are referenced to a Rubidium clock, which in turn is referenced to a GPS signal to compensate long term drifts. The Allan deviation of the Rubidium clock is specified to be 2×10^{-11} at 1 s.

⁶Since we use the doubled light, the comb has twice the CEO of the original comb.

Finally, we can compute the relative stability.

$$\Delta_{rel} = 2\beta\Delta f_{CEO} + \beta\Delta f_M \quad (4.35)$$

Since $\beta < 1$, the relative stability is actually better than the stability of the master, at least in the optimal case of $\Delta f_{CEO} = 0$. However, it is important to note that the more relevant fractional relative stability will be the same as the fractional stability for the master laser.

$$\frac{\Delta_{rel}}{f_M - f_S} = \frac{\Delta f_M}{f_M} \quad (4.36)$$

In fact, the fractional stability is the metrological quantity that is inherited in all locking schemes. This is also the reason why one uses an optical references instead of simply locking f_{RR} to an RF clock: The fractional stability of our clock laser at short time scales is $\mathcal{O}(10^4)$ times better than the stability of the Rubidium clock in our lab.

4.3.3 CEO Subtraction

As discussed in the previous section, the f_{RR} lock has a high enough bandwidth to achieve a proper phase lock, which is why we neglected Δf_{RR} in the stability calculation. f_{CEO} is also phase locked to a stable RF reference, but since the fast feedback branch (EOM) is reserved for f_{RR} , the CEO locking bandwidth (pump current feedback) is limited to ~ 5 kHz. According to Menlo, this is not enough to implement proper phase locking and thus leads to a very broad CEO linewidth of $\Delta f_{CEO} \sim 100$ kHz. According to equation 4.34, this heavily impairs the stability transfer and would impose a limit of $\Delta f_S \sim 10$ kHz for our current wavelengths.

Menlo therefore includes the option for a CEO subtraction lock. The idea is that the comb has a very well defined spacing (f_{RR}), but a jittering offset (f_{CEO}). However, the comb appears completely stable in a jittering reference frame. If f_{CEO} is subtracted from all beat notes, one jumps exactly in this jittering reference frame. If we subtract f_{CEO} from equation 4.31 and 4.32 and carry out the following calculation, Δf_{CEO} does not contribute to the relative stability anymore.

Unfortunately, Menlo only includes single CEO subtraction, while we would have to subtract $2f_{CEO}$ since we use a frequency doubled comb. Attempts to modify the internal locking electronics of the comb by e.g. dividing the beat notes by two before mixing with the CEO failed, since it was not possible to achieve sufficient signal to noise ratios (SNR).⁷

⁷The internal band pass filters and amplifiers are all optimized for specific locking schemes and frequencies.

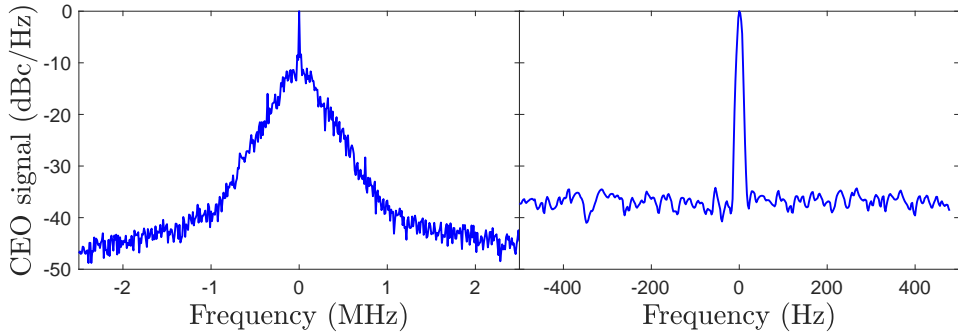


Figure 4.14: CEO signal measured with a bandwidth of 1 kHz (left) and 10 Hz (right).
The center is at 20 MHz.

With the construction of the new clock laser we finally obtained an independent way to evaluate the stability transfer and we decided to examine the CEO signal and different subtraction schemes more closely.

Surprisingly, the CEO turned out to be much narrower than expected when we measured it on a spectrum analyzer with smaller bandwidth than the one integral to the comb rack (delivered by Menlo). Indeed there is a broad background with a width of ~ 260 kHz, but a very narrow feature (limited by the 10 Hz bandwidth) can be measured, which has very high SNR and doesn't stem from RF leakage (see figure 4.14). Since the SNR of the narrow peak is > 30 dB, one could suspect that the CEO subtraction doesn't matter at all.

To test different subtraction schemes, f_{RR} is locked to A laser at 689 nm and a beat note with the new clock laser α is observed.⁸ Note that the same subtraction is performed on both laser beat notes with the comb.

The results are depicted in figure 4.15. In order to subtract the CEO twice, we use a feed forward scheme. The CEO signal is frequency doubled and fed to an AOM. The master laser passes the AOM in first order and therefore the CEO cancels out in the beat note with the comb. The different schemes are explained in table 4.2.

The conclusion we draw from this test is that the CEO subtraction hardly seems to matter at all, as expected from the narrow feature in the CEO signal (figure 4.14). For all schemes a very narrow feature is visible, which has the same width (~ 200 Hz) for all schemes. The much broader pedestal has a width of ~ 100 kHz, close to the width of the CEO pedestal. However, there's no notable difference between the schemes with 0xCEO and 1xCEO subtraction, except for the SNR. Most likely, the different SNR is

⁸This is the same scheme used to evaluate the locking performance of the new clock laser in section 4.1.

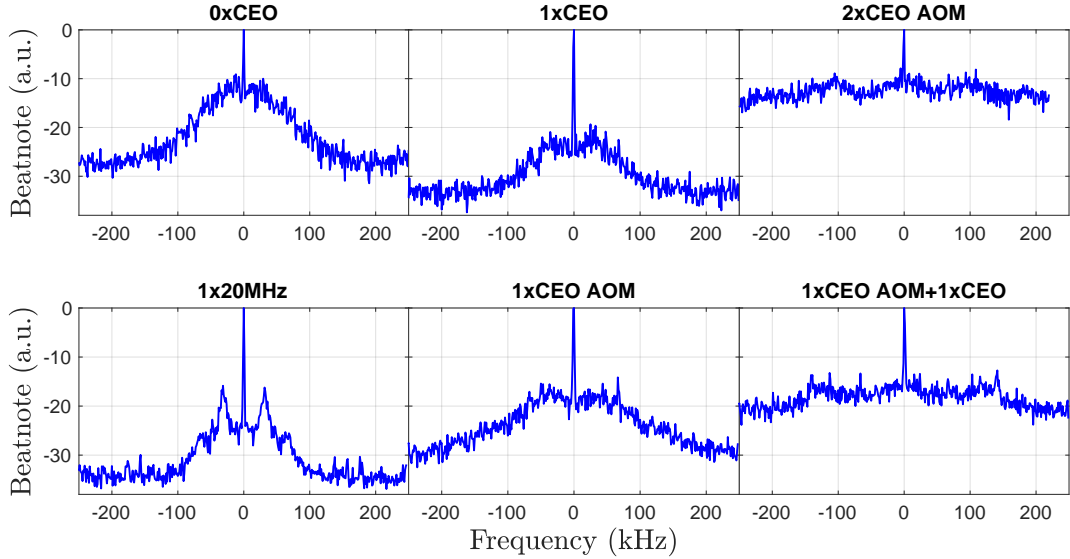


Figure 4.15: Beat note between comb and the new clock laser for different CEO subtraction schemes.

just a manifestation of different SNRs of the f_{RR} error signal, leading to a better overall lock. This becomes evident if the 1x20 MHz scheme is examined. This scheme doesn't subtract the CEO, but uses the same filters and amplifiers as the 1xCEO subtraction scheme. Since this control scheme appears to yield very similar locking performance as the 1xCEO scheme, it seems likely that the differences only arise due to different SNRs of the error signal.

The schemes with 2xCEO subtraction exhibit a qualitatively different pedestal, which could indicate that the CEO is indeed fully subtracted. Nonetheless, the pedestal

Scheme	Explanation	Subtraction
0xCEO	Standard scheme	0x
1x20 MHz	Menlo scheme for CEO subtraction, CEO replaced by 20 MHz signal from a DDS	0x
1xCEO	Single CEO subtraction using the Menlo scheme	1x
1XCEO AOM	Single CEO subtraction using an AOM	1x
2xCEO AOM	Double CEO subtraction using an AOM	2x
1xCEO AOM +1xCEO	Single subtraction using the Menlo scheme & single subtraction using an AOM	2x

Table 4.2: Explanation of the different CEO subtraction schemes.

suppression is worse than for the other schemes. A better solution for the AOM subtraction would be a double pass configuration, since it is less sensitive to alignment and no frequency doubling is needed. Frequency doubling introduces harmonics which weren't filtered out with appropriate band pass filters. Unfortunately, setting up a double pass would have required major changes in the optical setup for an otherwise relatively quick test, but for future tests it should be the preferred solution.

In conclusion, the combs performance seems to be much better than specified by Menlo. Indeed, the company was rather surprised to see these results. It seems to be reasonable to continue without CEO subtraction (or even use the 1x20 MHz scheme) and simply optimize the error signal to be as clean as possible. Ultimately, the best test would be to scan a narrow two-photon resonance and compare the different schemes.

4.3.4 Metrology with a Frequency Comb

Once a very good relative stability between the two Raman lasers is achieved, one can precisely measure the energy differences of the vibrational levels in the ground state potential. The energy difference is simply given by the difference between the two laser frequencies f_1 and f_2 :

$$\Delta\nu = f_2 - f_1 = (n_2 - n_1)f_{RR} - \delta_2 + \delta_1 \quad (4.37)$$

where f_1 and f_2 have been substituted using equation 4.31 and 4.32. $n_{1,2}$ label the comb teeth closest to $f_{1,2}$ and $\delta_{1,2}$ include all frequency offsets between the lasers and the comb teeth $n_{1,2}$. These offsets include a locking offset to the next comb tooth, double pass AOM frequencies, offsets due to the FNC AOM and a shutter AOM offset. For f_1 , there is an additional offset, since it is phase locked to the master laser. It is very important to include all these frequencies with the correct sign.

Determination of the Comb Tooth Number n

To calculate $\Delta\nu$ using equation 4.37, one first has to determine the comb tooth numbers n_1 and n_2 . The simplest way is to use a wave meter to obtain an estimate for the laser frequency f_L . The beat note between comb and laser is given by:

$$\delta = 2f_{CEO} + nf_{RR} - f_L \quad (4.38)$$

$$n = \frac{\delta - 2f_{CEO} + f_L}{f_{RR}} \quad (4.39)$$

As an example we take the α laser and our current setup. Note that the CEO has a negative value (per definition). The relevant numbers are $\delta = 60 \text{ MHz}$, $f_{CEO} = -20 \text{ MHz}$, $f_L = 384.585\,04(3) \text{ THz}$ and $f_{RR} = 250.014\,367\,401(1) \text{ MHz}$, giving $n = 1\,538\,252.14(24)$. Since our blue MOT laser is locked to the Sr $^1S_0 \rightarrow ^1P_1$ transition, which is very well known, we can use this information to calibrate the frequency offset of the wave meter. On this particular day, an offset of 35 MHz was calculated, leading to $n = 1538252.0002$, which is even closer to an integer. This method was repeated for the 689 nm laser on different days, giving similar results and indicating that the calibration method works very well.

Clock Operation

Once the comb teeth are known, one has to constantly count the repetition rate while the two-photon transition is scanned and the lasers are held on resonance by adjusting the AOM frequencies. Using equation 4.37, a time series of frequencies is obtained. One then operates the clock for a long time, $\mathcal{O}(d)$, to average and obtain a smaller statistical error.

In addition, systematic effects such as black body radiation, Raman light shifts, residual lattice shifts, magnetic field, density, residual Doppler shift, etc. have to be precisely measured, controlled and compensated for in the final result.

5 Autler-Townes Spectroscopy of Deeply Bound Ground States

The experiments outlined in section 1.1 require precise metrology of the vibrational levels in the ground state potential. Since $\langle v_1 | v_2 \rangle = 0$ in diatomic, homonuclear molecules and the binding energies of deeply bound states are in the THz regime, one has to use two-photon transitions for spectroscopy.

In order to find the deeply bound states, Autler-Townes spectroscopy is employed.

5.1 Lambda Scheme

In our case we want to drive a transition between two vibrational states in the ground state potential via some intermediate state in the excited 0_u^+ potential (see figure 3.2). This system is effectively a three-level lambda system, since the Rabi rates are small compared to the vibrational spacing.

If we define the zero energy at the deepest level, the Hamiltonian of the system in figure 5.1 is given by equation 5.1 (in the rotating wave approximation) [46].

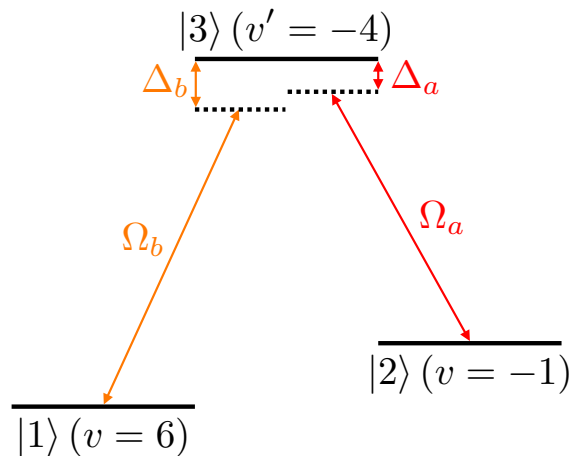


Figure 5.1: Three-level system in lambda configuration. The zero energy point is chosen at the deepest state $v = 6$.

$$\hat{H} = \frac{\hbar}{2} \begin{bmatrix} 0 & 0 & \Omega_b \\ 0 & 2\delta & \Omega_a \\ \Omega_b & \Omega_a & 2\Delta \end{bmatrix} \quad (5.1)$$

where the detunings are defined as $\Delta = \Delta_b$ and $\delta = \Delta_b - \Delta_a$ to simplify the matrix. Let's further simplify the matrix by assuming two-photon resonance: $\Delta_a = \Delta_b$, i.e. $\delta = 0$. When we compute the eigenvalues of this Hamiltonian, one notices that one of the eigenvalues is still the same as in the uncoupled case. The other two eigenvalues are split by the off-diagonal interaction terms:

$$E_0 = 0$$

$$E_{\pm} = \frac{\hbar}{2}(\Delta \pm \sqrt{\Delta^2 + \Omega_a^2 + \Omega_b^2}) \quad (5.2)$$

Even for zero detuning $\Delta = 0$, these so-called "dressed" states are still split by the Rabi frequencies. This effect is called Autler-Townes splitting and can be used to spectroscopically locate deeply bound states [47].

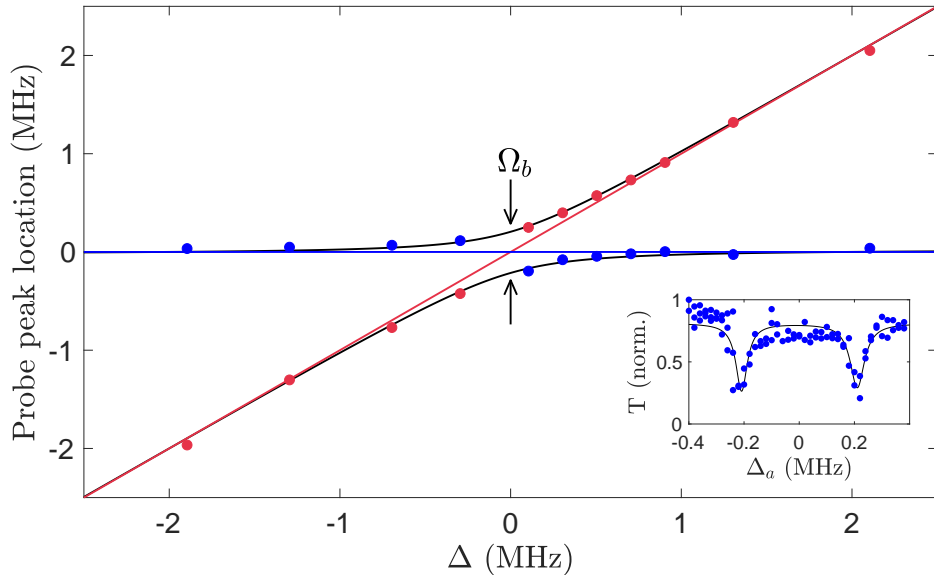


Figure 5.2: Autler-Townes peak locations for the deeply bound state $X(6,0)$. For each detuning Δ , the probe laser is swept to obtain an absorption spectrum (an example is shown in the inset). The peaks are fitted and the peak location is plotted against Δ . The red and blue lines represent the uncoupled system. Red symbolizes the two-photon transition and blue the one-photon peaks.

In order to find these states, one "parks" a weak ($\Omega_a \ll \Omega_b$) probe laser on resonance with the excited state and then searches with a strong pump laser in the vicinity of the expected transition. Once the pump laser hits the resonance, Autler-Townes splitting will occur and thus lift the probe absorption. In order to find the resonance, the shift has to be larger than twice the linewidth of the probe.

$$\frac{\Delta \pm \sqrt{\Omega_a^2 + \Omega_b^2 + \Delta^2}}{2} > 2\Gamma \quad (5.3)$$

To increase the sensitivity of this scheme, one therefore has to maximize the pump Rabi frequency Ω_b and thus its power. Also, the method is more sensitive for states with a larger dipole matrix element and Franck-Condon factor, as well as for a narrower probe transition. For the states and laser powers in question, the condition reads $\Delta > \mathcal{O}(10 \text{ MHz})$, i.e. one can search with a relatively large step size of $\mathcal{O}(1 \text{ MHz})$. Once the resonance is found, one can measure the splitting as a function of Δ and obtain the avoided crossing depicted in figure 5.2.

Adiabatic Elimination

The eigenstates of the coupled three-level system are superpositions of the bare eigenstates and can be expressed by mixing angles θ and ϕ .

$$\begin{aligned} |a_0\rangle &= \cos(\theta) |1\rangle - \sin(\theta) |2\rangle \\ |a_+\rangle &= \sin(\theta)\sin(\phi) |1\rangle + \cos(\theta)\sin(\phi) |2\rangle + \cos(\phi) |3\rangle \\ |a_-\rangle &= \sin(\theta)\cos(\phi) |1\rangle + \cos(\theta)\cos(\phi) |2\rangle - \sin(\phi) |3\rangle \end{aligned} \quad (5.4)$$

The mixing angles are given by:

$$\tan(\theta) = -\frac{\Omega_b}{\Omega_a} \quad \tan(2\phi) = \frac{-\sqrt{\Omega_a^2 + \Omega_b^2}}{\Delta} \quad (5.5)$$

For large detuning $\Delta \gg \sqrt{\Omega_a^2 + \Omega_b^2}$, $\phi \rightarrow 0$ and the eigenstates simplify:

$$\begin{aligned} |a_0\rangle &= \cos(\theta) |1\rangle - \sin(\theta) |2\rangle \\ |a_+\rangle &= |3\rangle \\ |a_-\rangle &= \sin(\theta) |1\rangle + \cos(\theta) |2\rangle \end{aligned} \quad (5.6)$$

The bare eigenstate $|3\rangle$ is now also an eigenstate of the coupled system, i.e. a stationary state. This hints at why the intermediate state can be adiabatically eliminated. $|3\rangle$ is essentially a dark state and its population does not change. Heuristically, this means that two photons are absorbed coherently without creating population in the intermediate state $|3\rangle$.

In the Schrödinger picture we can write for the c_i coordinates in the uncoupled basis:

$$i\hbar \frac{\partial}{\partial t} \begin{bmatrix} c_1 \\ c_2 \\ c_3 \end{bmatrix} = \frac{\hbar}{2} \begin{bmatrix} \Omega_b c_3 \\ 2\delta c_2 + \Omega_a c_3 \\ \Omega_b c_1 + \Omega_a c_2 + 2\Delta c_3 \end{bmatrix} \quad (5.7)$$

For the large detuning limit, we now set $\dot{c}_3 = 0$, since $|3\rangle$ is a stationary state. Solving for c_3 and reinserting into the two remaining equations yields an effective Hamiltonian in the now reduced system:

$$\hat{H}_{eff} = -\frac{\hbar}{2} \begin{bmatrix} \frac{\Omega_b^2}{2\Delta} & \frac{\Omega_a \Omega_b}{2\Delta} \\ \frac{\Omega_a \Omega_b}{2\Delta} & \frac{\Omega_a^2}{2\Delta} - 2\delta \end{bmatrix} \quad (5.8)$$

Comparing to a two-level system, one obtains an effective Rabi rate:

$$\Omega_{eff} = \frac{\Omega_a \Omega_b}{2\Delta} \quad (5.9)$$

The diagonal terms describe the Stark shifts. The differential light shift on resonance is thus given by:

$$\Delta\omega_{diff} = \frac{1}{4\Delta} (\Omega_b^2 - \Omega_a^2) \quad (5.10)$$

This approximation is called adiabatic elimination [48]. The resonance that satisfies this approximation will be called "two-photon resonance" in the further discussion. Since excited state population leads to increased scattering and light shifts, the clock transition will be operated in this regime, where $\Delta \gg \sqrt{\Omega_a^2 + \Omega_b^2}$.

5.2 Binding Energies

Several deeply bound states $X(v, 0)$ are accessible with our current lasers and are located using the method described above. Using Autler-Townes spectroscopy, one can obtain a simple estimate of the binding energy of the states. For this quick measurement, we simply rely on the wave meter and previous measurements, without involving the frequency comb. Therefore, the error is on the order of 30 MHz. We transfer the molecules via the intermediate state $0_u^+(-4, 1)$, which has a measured binding energy

v	Experiment (THz)	Theory (THz)	Deviation (MHz)
8	23.0130	23.0135	500
7	24.0311	24.0317	600
6	25.0728	25.0736	800
5	26.1386	26.1393	700
4	27.2282	27.2288	600

Table 5.1: Comparison between experimental and theoretical binding energies for the deeply bound ground states $X(v, 0)$.

of 1084.093(33) MHz. Together with the intercombination line at 14 504.35 cm, we can calculate the binding energy:

$$\frac{E_b(v = n)}{\hbar} = \omega_b + \frac{E_b(v' = -4)}{\hbar} - \omega_{\text{intercombination}} \quad (5.11)$$

Table 5.1 shows the measured binding energies compared to theoretical values, which were calculated by Iwona Majewska and Robert Moszynski using data obtained by Fourier transform spectroscopy to scale the potential [49]. The data is in excellent agreement with these calculations, with deviations of less than 1 GHz for all observed states, corresponding to only 0.004 %.

This should only be taken as a quick consistency check, since the observed linewidths are still relatively large. The actual metrology will be performed as described in chapter 4.3.4. The narrowest two-photon resonance that we observed with this setup has a width of 70 kHz. The dominant broadening mechanism is the inhomogeneous AC stark shift induced by the lattice laser. In order to eliminate this effect, one can use a so-called magic wavelength, at which the differential light shift of two states is eliminated altogether.

6 Magic Wavelength Spectroscopy

6.1 Polarizability

The polarizability α is the proportionality constant relating dipole moment and electric field and leads to an intensity-dependent energy shift. It is in general not the same for different molecular states. Therefore, molecules in different states experience a different lattice potential and light shift.

Together with the inhomogeneous trap, this leads to a broadening of $\sim 70\text{ kHz}$ for the two-photon transition and also introduces a large systematic error. The transition frequency experiences a shift of $\Delta\omega_0$ [50]:

$$\Delta\omega_0 = -\frac{1}{2}(\alpha_1 - \alpha_2)|\mathbf{E}|^2 \quad (6.1)$$

where α_1 and α_2 are the polarizabilities of the two states.

Since the molecular polarizability is frequency-dependent, one can tune the polarizability of one of the states close to some molecular transition. It is thus possible to match α_1 and α_2 so that the differential light shift $\Delta\omega_0$ becomes zero.

The polarizability close to resonance can be calculated by taking the steady state expectation value of the dipole operator, which is directly related to the polarizability. The energy shift considering only a single transition (including damping) is then given by:

$$\Delta\omega = -\frac{1}{2}\alpha|\mathbf{E}|^2 = \frac{\Delta\Omega^2}{\Omega^2/2 + \Delta^2 + \gamma^2/4} = \quad (6.2)$$

where γ is the natural linewidth. A derivation can be found in appendix A.2.

By measuring the peak location as a function of lattice detuning, one can observe the polarizability resonance, as illustrated in figure 6.1.

6.2 Magic Wavelength

Currently, we have a lattice laser that is tunable between $\sim 905\text{-}925\text{ nm}$. The strongest transitions accessible in this range connect the deeply bound states $X(v = 4 - 8, 0)$ with the 1_u potential.

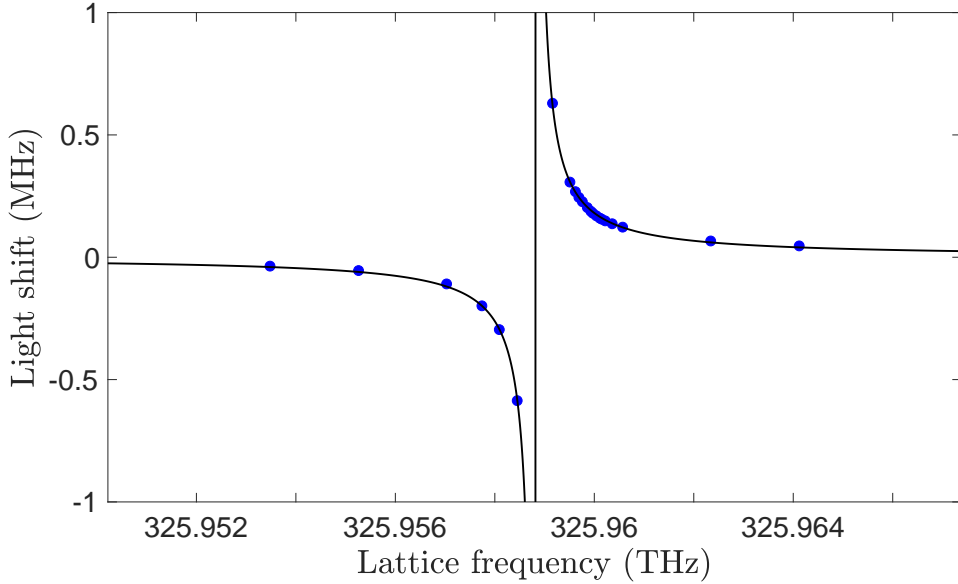


Figure 6.1: Lattice light shift near the $1u(20,1)$ resonance. The error bars are smaller than the data points.

In order to find these states, we employ a similar method as described in chapter 5. The two Raman lasers are parked on the two-photon resonance and the lattice is swept with maximum intensity. When the lattice is close to resonance, it will shift the two-photon resonance by $\Delta\omega_0$ and a rise in the recovery signal is observed. Figure 6.1 shows this shift as a function of the lattice frequency. By fitting to equation 6.1, we obtain the Rabi frequency and can calculate the dipole matrix element squared (dms in table 6.1). The dms is obtained using the following formulas [51]:

$$\Omega = \frac{1}{\hbar} \sqrt{dms} E_0 \quad (6.3)$$

$$E_0^2 = \frac{4P}{c\epsilon_0\pi w_0^2} \quad (6.4)$$

where P and w_0 are the total power and waist of the Gaussian lattice profile respectively and the extra factor of 2 comes from the retro-reflected lattice beam. For the fit, γ is set to zero, since $\gamma \ll \Omega$.¹

The theoretical predictions for the transition frequencies is very close to the experimen-

¹Note that the fit gives the same Ω within error even if γ is included as a fixed parameter or as a fit parameter.

tal value, although worse than for the ground state potential. The mean deviation is ~ 500 GHz, corresponding to $\sim 0.1\%$. Note that the experimental error is again limited by the wavemeter, to ~ 30 MHz. The calculations of the dms however differ much further from our measurements. The calculated value is larger by a factor of 800 on average. A comparison to the theoretical values can be found in table 6.1.

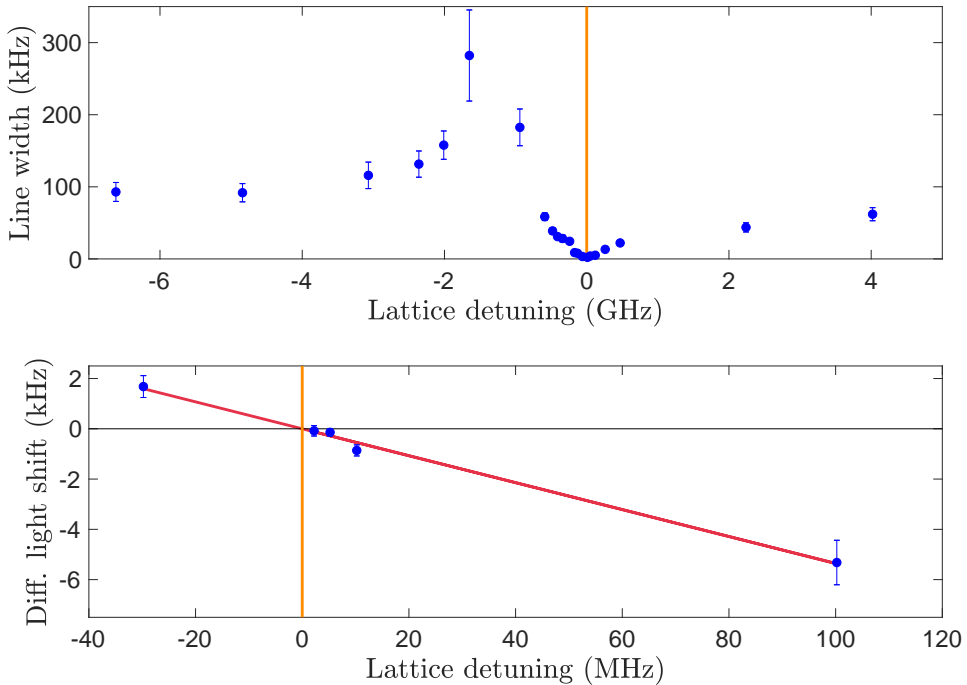


Figure 6.2: **Top:** The linewidth of the two-photon resonance features a minimum at the magic wavelength, indicated by the orange line.
Bottom: By taking the difference between the light shifts for two different lattice intensities, one can measure the magic wavelength as a zero-crossing in the difference of the two shifts.

Once we have found the resonance, we use two distinct methods to determine the exact magic wavelength. At the magic wavelength, the inhomogeneous broadening is lifted and the linewidth features a minimum, as can be seen in the top part of figure 6.2. In addition, one can measure the shift for two different lattice intensities and then subtract the two shifts. At the magic wavelength, the shift is not power-dependent anymore, since $\alpha_1 - \alpha_2 = 0$. Therefore, the zero-crossing in the bottom part of figure 6.2 corresponds to the magic wavelength. We locate four resonances suitable to implement

v'	f_{exp} (THz)	f_{th} (THz)	$dms_{exp}(ea_0)^2$	$dms_{th}(ea_0)^2$
22	330.3181	330.902	4.50×10^{-8}	1.13×10^{-4}
21	328.1452	328.684	1.62×10^{-7}	9.70×10^{-5}
20	325.9588	326.465	2.90×10^{-7}	4.18×10^{-5}
19	323.9836	324.247	3.29×10^{-7}	1.51×10^{-6}

Table 6.1: Comparison between experiment and theory for the transitions $X(6,0) \leftrightarrow 1_u(v',1)$. The mean deviation of the transition frequencies is ~ 500 GHz, i.e. the calculations are much further off than for the ground state levels. For the dms values, the deviation is much worse, the theoretical value is larger by a factor of 800 on average.

this magic wavelength scheme (see table 6.1).

In comparison to the resonances typically used for atomic magic wavelengths, the transition strengths are much smaller. This leads to several challenges. For the following discussion we will focus only on the strongest transition, $X(6,0) \leftrightarrow 1_u(19,1)$.

Lattice Stabilization

In the past, the lattice laser was locked to a wave meter with a resolution of 30 MHz. Since the wave meter has a very small readout rate, the servo bandwidth is limited to several Hz. Because the resonance is relatively steep at the magic wavelength, a jittering lattice laser leads to an uncertainty in the light shift:

$$\delta\omega_0 = \frac{d\Delta\omega_0}{d\omega} \cdot \gamma_L = 5 \times 10^{-5} \cdot \gamma \quad (6.5)$$

where γ_L is the linewidth or jitter of the lattice laser. In other words, in order to suppress the broadening described by equation 6.5, one has to decrease the linewidth of the lattice laser. To achieve only 1 Hz uncertainty, the laser linewidth has to be < 20 kHz. Since we have already locked our frequency comb to an ultra stable laser (section 4.1), we can simply lock the lattice to the comb as well and ensure $\gamma_L \sim 200$ Hz. The broadening $\delta\omega_0$ due to the lattice linewidth is then limited to 10 mHz.

6.2.1 Off-Resonant Scattering

The scattering rate close to resonance is given by (derivation in A.2):

$$\Gamma = \frac{\gamma\Omega^2}{2\Omega^2 + 4\Delta^2 + \gamma^2} \quad (6.6)$$

Since the transition is not very strong, one finds the magic wavelength only 1.2 GHz away from resonance. For a lattice intensity of 230 mW and a beam waist of 29 μm this leads to a scattering rate of 0.14 Hz, imposing an upper limit on the linewidth that can possibly be achieved for the two-photon transition.

Unfortunately, this calculation depends basically linearly on γ , which couldn't be obtained from the fit, since γ is much smaller than Ω and we did not obtain data for the turnaround of the polarizability resonance in figure 6.1. We therefore rely on the theoretical value of ~ 3 kHz. Considering the large deviations of the theoretical values for the *dms*, it is unclear how much this scattering rate is to be trusted.

A superior method to estimate the lattice-induced scattering rate is to measure the lifetime of the deeply bound state, see chapter 7.

6.2.2 TA Pedestal

In order to achieve a high lattice power, an ECDL is used to seed a TA chip. A common complication of this setup is that the TA output spectrum features a very broad pedestal caused by amplified spontaneous emission (ASE) [52]. The ASE pedestal is ~ 20 nm wide and typically $\mathcal{O}(10^2)$ weaker in power than the central peak. As we have to operate at relatively small detuning, the pedestal fully covers at least three vibrational transitions, leading to increased scattering rates.

Since the ASE background is typically multi-mode and we couple the lattice light into a single-mode fiber, some filtering is achieved. In addition, a transmission grating is installed before the fiber to spectrally spread the pedestal and alleviate the problem. Another possibility would be to lock a Fabry-Perot cavity to the laser and to only use the transmitted light, which would reduce the ASE power by the cavity finesse \mathcal{F} .

The effect of the TA pedestal on the ground state lifetime is currently being investigated in the lab and it is yet unclear how successful the filtering will be. If ASE turns out to fundamentally limit the clock performance, one could replace the current lattice setup with a Titanium-Sapphire laser, which yields high power and large tunability without the need for spectral filtering.

6.3 Current Limitations

Using the magic wavelength technique, it was possible to narrow the two-photon transition from ~ 70 kHz down to 160 Hz, corresponding to an ~ 400 -fold improvement in coherence (see figure 6.3).

The limiting factor for this width is still under investigation at the time of writing, but

in the following, possible limits and how they could be overcome will be discussed.

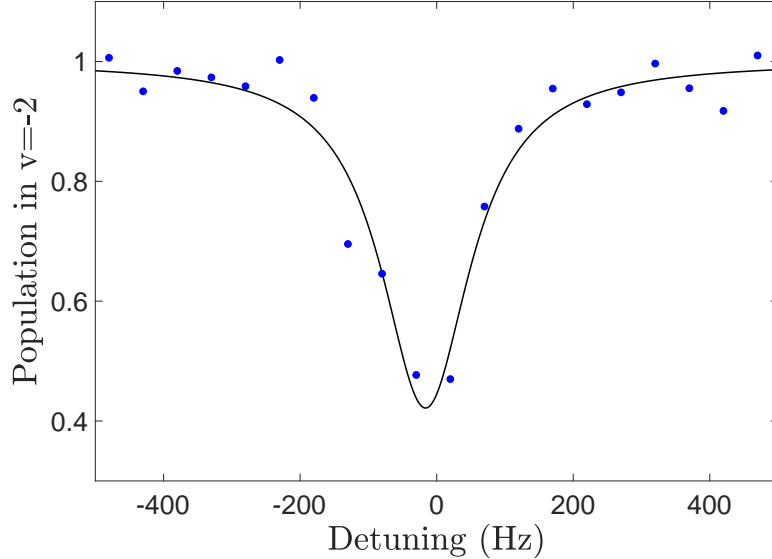


Figure 6.3: Narrow two-photon resonance. The Lorentzian fit yields a linewidth of 159 Hz.

1. **Lattice scattering:** As described in the previous section, the ASE-induced scattering could be reduced by further filtering or by replacing the lattice laser with a Titanium-Sapphire laser. Additionally, it might become necessary to look for a stronger transition to implement the magic wavelength. According to the lifetime measurements of the deeply bound states (chapter 7), this effect should broaden by ~ 25 Hz. Indeed, the two-photon linewidth of 160 Hz seems to be independent of lattice intensity so far.
2. **Probe laser scattering:** Just like the lattice laser, the Raman lasers can also induce scattering, because they are relatively close to the intermediate state in the 0_u^+ potential. This problem is easily resolved by far detuning compared to the Rabi frequencies (adiabatic elimination, see section 5.1).
3. **Natural linewidth:** Since we address states in the ground state potential, the natural lifetime should be very large. Indeed, for the shallow bound states, lifetimes of ~ 1 s have been observed and they should be similar for the more deeply bound states.

4. **Laser linewidth:** As discussed in section 4.3.2, the relative stability should be better than the laser linewidth by the factor $\beta = 1 - \frac{\omega_1}{\omega_2}$. For the measured laser linewidth of < 200 Hz and the current Raman frequencies, the relative linewidth should be ~ 10 Hz. Unfortunately, we currently don't have an independent way to measure the relative width, which is why the laser linewidth cannot be fully ruled out to explain the 160 Hz resonance width. Anyhow, the integration of the new clock laser should improve both short-term and long-term laser stability by at least one order of magnitude.
5. **Raman laser intensities:** The Stark shift introduced by the Raman lasers can also broaden the lines due to power fluctuations and an inhomogeneous laser profile and can cause a large systematic error. Since the sign of the shift is the same for both lasers, one can cancel the differential shift by choosing an appropriate power balance. Additionally, the power stabilization to $< 0.1\%$ described in section 4.2 allows for precise control of systematic shifts. The inhomogeneity can be circumvented by making the Raman beams much larger than the optical lattice.
6. **Density:** The density can be controlled both by the ^{88}Sr loading time and the photoassociation pulse time. No density-dependent effects have been observed so far.
7. **Transverse Doppler shift:** In practice, perfect alignment of the Raman beams and the lattice will not be achieved. For an offset angle ϵ , a residual Doppler broadening of $\Delta_{\text{res}} = \sin(\epsilon)\Delta_D$ will persist, where Δ_D is the Doppler broadening due to the transverse temperature in the dipole trap. This broadening is ~ 1 Hz for an alignment of $\epsilon = 0.1^\circ$. Our setup profits from the co-aligned Raman beams which reduce the Doppler broadening in a lambda configuration.
8. **Magnetic field fluctuations:** Active feedback is implemented using compensation coils. In addition, the absence of nuclear spin and thus hyperfine structure in $^{88}\text{Sr}_2$ should significantly reduce this effect compared to e.g. ^{87}Sr atomic clocks.

In conclusion, it is not yet quite clear what the limiting factor for the 160 Hz linewidth is. In any case, it seems like lattice scattering caused by the broad ASE spectrum is currently a main obstacle towards Hz-level spectroscopy.

7 Coherent Transfer

7.1 Rabi Oscillation

As demonstrated in the last chapter, the coherence can be increased by two orders of magnitude using a magic wavelength to achieve a state-insensitive trapping potential. To show that the Raman transfer between vibrational levels in the ground state can be performed in a coherent way, one can drive Rabi oscillations between the two states. As described in section 5.1, the three-level system reduces to an effective two-level system for large detuning. The effective Rabi rate is then given by:

$$\Omega_{\text{eff}} = \frac{\Omega_a \Omega_b}{2\Delta} \quad (7.1)$$

To observe Rabi oscillations, the population in the shallow bound state is recorded as a function of Raman pulse time. After a so-called π -pulse, the molecules are fully transferred to the deeply bound state.

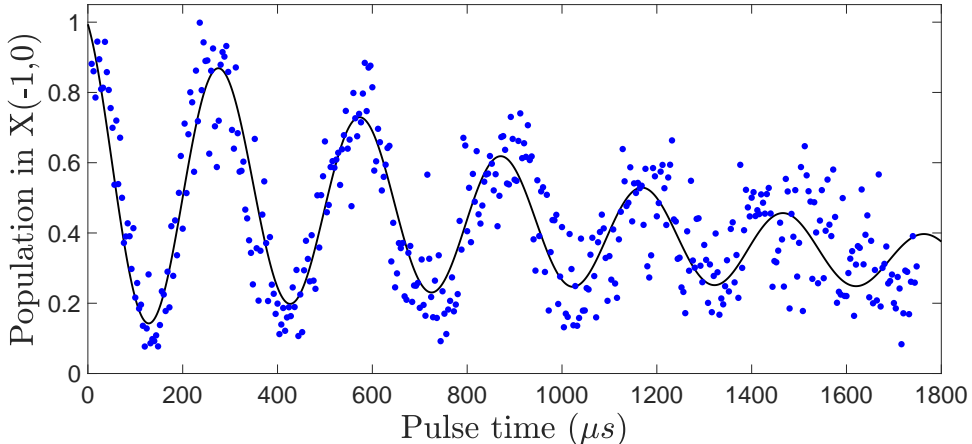


Figure 7.1: Rabi oscillations between $X(-1,0)$ and $X(6,0)$. The effective Rabi rate obtained from the fit is $\Omega_{\text{eff}} = 2\pi \cdot 3.4 \text{ kHz}$.

However, due to the final lifetime of the states and incoherence introduced by the

lasers and residual light shifts, the dynamics follows a damped sinusoidal oscillation, where the envelope's time scale is determined by the effective decoherence time of the system [51].¹ Figure 7.1 features several cycles of such an oscillation. Three revivals are clearly visible until the molecules dephase. In order to achieve a large enough Ω_{eff} , the Raman powers are significantly increased, leading to a larger intermediate state population. Since the decay from 0_u^+ is very fast and has many channels, this accelerates decoherence and thus explains the relatively small dephasing timescale of $\tau_2 = 979 \mu\text{s}$.

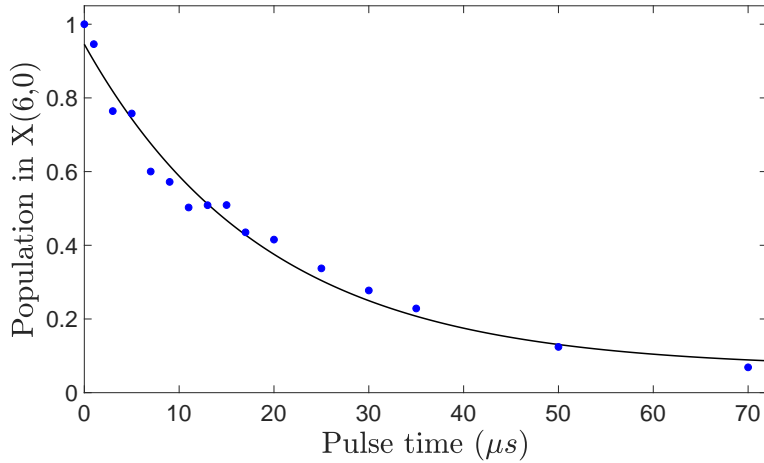


Figure 7.2: Lifetime measurement of $X(6,0)$. The exponential fit reveals a lifetime of 19.15 ms.

7.2 Lifetime Measurements

Once the π -pulse time is determined, it is possible to measure the lifetime of the deeply bound state without the need of a separate recovery laser. The lifetime of the two clock states is an ultimate limit to the linewidths that one can observe, since lifetime and linewidth are related via a Fourier uncertainty [51]:

$$\Delta\omega = \frac{1}{T} \quad (7.2)$$

The following sequence is used:

1. **π -pulse:** The molecules are transferred to the deeply bound state.

¹The data was fitted to the following function: $f(t) = A_1 e^{-t/\tau_1} + A_2 e^{-t/\tau_2} \sin[2\pi(x - x_0)\Omega_{\text{eff}}]$. The parameter τ_1 was introduced phenomenologically to account for residual intermediate state population.

2. **Wipe:** The molecules left in the shallow bound state are wiped away by a short recovery pulse.
3. **Wait:** The system is left in the deeply bound state for a variable amount of wait time.
4. **π -pulse:** The molecules are transferred back to the shallow bound state.
5. **Recovery:** The molecules in the shallow bound state are counted (see section 3.3).

The data in figure 7.2 is fit to an exponential function, yielding a lifetime of 19.15 ms for a moderate lattice power of 160 mW. This is much less than expected from the scattering rate calculation in section 6.6 ($\Gamma = 0.14 \text{ Hz}$).

Unfortunately, this measurement has not yet been fully repeatable although it seems like the main culprit are changes in the lattice TA pedestal. Tests with non-magic wavelengths have indicated that the pedestal could be the limiting factor for the relatively short lifetimes.

Therefore, the lab currently works towards improved spectral filtering of the lattice laser, paving the path to Hz-level spectroscopy, which we hope to achieve with the new clock laser and a next-generation Raman scheme. The new setup should allow access to the whole rovibrational spectrum of the ground state potential, as outlined in the next chapter.

8 Summary and Outlook

Several deeply bound vibrational levels in the ground state potential are located using Autler-Townes spectroscopy. By tuning the polarizability of one of the states, a magic wavelength is achieved. The coherence is increased by more than two orders of magnitude and it is possible to drive Rabi oscillations across almost the entire ground state potential. The narrowest observed linewidth for the two-photon resonance is 160 Hz. Several improvements are made on the technical side to further increase the spectroscopic precision.

A new clock laser is constructed, with an estimated linewidth of $\mathcal{O}(\text{Hz})$ and 390 mHz/s drift. Fiber noise cancellation and intensity stabilization are implemented for the two Raman lasers. In addition, the fiber carrying the clock laser light to the frequency comb is fiber noise canceled. The FNC systems support stability transfer on the order of 10^{-18} . Different locking schemes for the frequency comb are analyzed and compared in order to achieve optimal stability transfer between the Raman lasers.

In order to reduce lattice induced scattering, spectral filtering of the TA output is established.

The next step will be the integration of the new clock laser into the experiment. The wavelength of 780 nm is chosen so that the spectroscopy of the entire ground state potential becomes feasible. Figure 8.1 shows a heat map of the calculated transition strengths between ground state levels v and 0_u^+ levels v' . The new clock laser at 780 nm will serve as the first leg of the Raman transition, connecting $X(-1, 0) \leftrightarrow 0_u^+(14, 1)$. This is a relatively strong transition, comparable to the transition that is currently used as the first leg.

The advantage of this new scheme is that $0_u^+(14, 1)$ exhibits large transition dipole moments with almost all v states in the ground state potential. The transition strengths are expected to be at least $\mathcal{O}(10^3)$ stronger than for the previous intermediate state $0_u^+(-4, 1)$ for all v states. For the absolute ground state $X(0, 0)$ the transition should even be 10^{10} times stronger.

Spectroscopy of the entire ground state potential is therefore in reach without switching the first leg laser. The large transition strengths will drastically simplify Autler-Townes spectroscopy, since the splitting becomes much larger and one can therefore search with

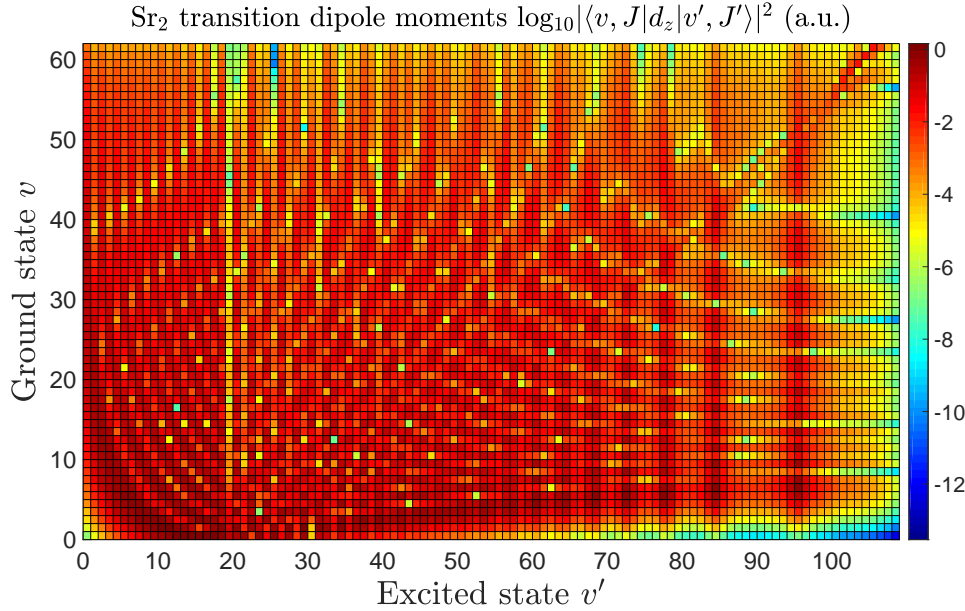


Figure 8.1: Heat map of the transition dipole moments between $X(v, 0)$ and $0_u^+(v', 1)$

a larger step size, according to equation 5.3.

The wavelength to reach $X(0, 0)$ is 720 nm and it should be possible to perform spectroscopy of the entire potential with three or four different ECDLs. Therefore, the entire optics setup for the second leg laser was fiber coupled, allowing a relatively quick switch between different wavelengths.

The increased frequency stability of the new clock laser and a spectrally filtered lattice spectrum should allow Hz-level spectroscopy of the vibrational levels in the ground state potential. To our knowledge, the highest quality factor to date for a molecular transition was measured in our lab for $E1$ forbidden subradiant states in $^{88}\text{Sr}_2$ [53]. With the new clock scheme we hope to surpass this record, opening new pathways for studies of fundamental physics: Searches for drifts in the electron-proton mass ratio and deviations from nano-scale Newtonian gravity with ultracold $^{88}\text{Sr}_2$ are in reach.

A Appendix

A.1 A Unibody Littman Laser

In practice, the response bandwidth of the laser as well as the servo bandwidth are typically limited to the order of 1 MHz. In order to lock to the narrow resonance of a high finesse cavity, one therefore needs a laser that has a sufficiently small linewidth to begin with, so that the feedback can effectively cancel phase noise across the whole laser spectrum.

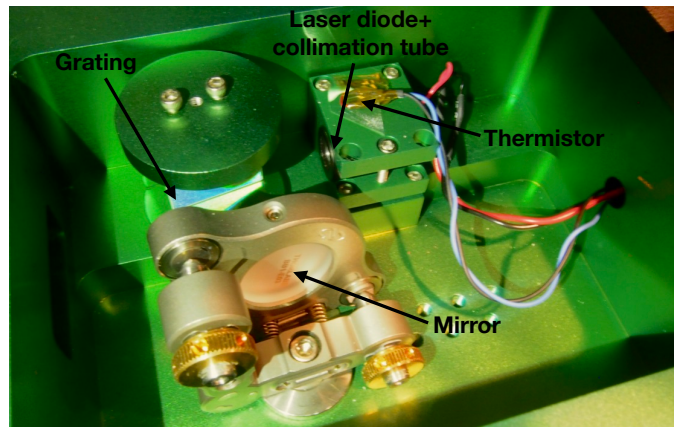


Figure A.1: Picture of the ECDL housing and the setup in Littman geometry. The grating can be turned and is fastened using an external screw.

Laser diodes are commonly used, but their internal resonator is usually very short, which translates to broad resonances and a line-width on the order of 100 MHz. An elegant way to improve these properties is an external cavity diode laser (ECDL), especially if wavelength tunability is important.

The design by Stanimir Kondov employs the Littman-Metcalf configuration [54, 55]. The output of the laser diode is collimated and incident on an external grating. The 0th order of the grating leaves the ECDL housing, while the 1st order gets reflected back by a mirror. The mirror forms an external cavity with the output facet of the laser diode. In

Component	Part number	Manufacturer
Laser diode	SAL-780-060	Sacher Lasertechnik
Collimation tube	LT230P-B	Thorlabs
Grating	GR25-1208	Thorlabs
Mirror	BB1-EO3	Thorlabs
Mirror mount	SS100T-F2H	Newport
TEC	TECF1S	Thorlabs
Thermistor	ATH10KR8 or TH10K	Analog Technologies or Thorlabs

Table A.1: Parts list for the construction of an ECDL in Littman-Metcalf configuration.

order to achieve single mode lasing, the external and internal modes have to overlap, leading to mode competition. This increases the wavelength selectivity of a single mode, resulting in spectral narrowing. Since tuning the mirror changes the wavelength that is fed back to the laser diode, one can tune the ECDL's wavelength by changing the mirror angle. The Littman-Metcalf configuration was chosen over a Littrow configuration, since it features larger wavelength selectivity and therefore smaller linewidth. This is because the light diffracts twice on the grating during a external cavity round trip. In addition, the alignment of the output beam is invariant to wavelength tuning, since it is formed by the 0th order of the grating. A drawback is the lower power output, but only very small powers are necessary for PDH locking anyway.

The ECDL consists of a uni-body aluminium housing, giving the design a large thermal mass which is important for temperature stability. The temperature is regulated by three thermo-electric coolers (TEC) connected in series, that are placed between the housing and an aluminium base plate. The temperature is measured through a thermistor enclosed in a small hole inside the laser diode holder. Both current and temperature control are performed by a commercial laser controller from Vescent Photonics (Model D2-105). The controller is also capable of two-stage temperature control. Thermal stability could be increased further by placing a second TEC directly between housing and laser diode holder and using a second thermistor to monitor the temperature of the housing. Figure A.1 shows the inside of the ECDL housing, containing a mount for the laser diode and a collimation tube, the grating and a mirror. A list of the parts being used can be found in table A.1.

With the current setup, the laser frequency doesn't deviate by more than 100 MHz in a 24 h period. The power output of 40 mW is more than enough for the PDH lock, which uses < 100 μ W.

A.2 Polarizability and Scattering Rate

Strictly speaking one would have to consider the full four-level system to calculate the dynamic polarizability change due to the near-resonant lattice. However, since the detuning is much larger than the Rabi rates, we will assume a simple two-level system for the calculation. The Hamiltonian can then be written as:

$$\hat{H} = \frac{\hbar}{2} \begin{bmatrix} 0 & \Omega \\ \Omega & 2\Delta \end{bmatrix} \quad (\text{A.1})$$

where Ω and Δ are the Rabi frequency and lattice detuning respectively.

The zero-energy point is chosen at the ground state energy and we used the rotating wave approximation.

The time evolution of the density matrix is given by the commutator of Hamiltonian and density matrix plus an additional term describing the dissipation of the system.

$$\dot{\rho} = -\frac{i}{\hbar} [\hat{H}, \rho] + \hat{\mathcal{L}}\rho \quad (\text{A.2})$$

Equation A.2 is called the master equation for an open quantum system. The first term describes coherent evolution of the closed system, whereas the second term includes decoherence terms. $\hat{\mathcal{L}}$ is called the Lindblad operator, or dissipator. In our case we want to describe spontaneous decay of the excited state in the 1_u potential. This process is described by the following dissipator:

$$\hat{\mathcal{L}} = \begin{bmatrix} -\gamma & -\gamma/2 \\ -\gamma/2 & -\gamma \end{bmatrix} \quad (\text{A.3})$$

The diagonal terms simply describe a decay of the population to the ground state, with a rate γ . The off-diagonal terms can be obtained by demanding trace preservation for ρ (A more rigorous justification of equation A.3 is explained in [56]).

For the two-level system, it is easy to find an analytical steady state solution for the density matrix, by setting $\dot{\rho} = 0$. One can then compute the expectation value of the dipole operator in the steady state:

$$\langle \hat{d} \rangle = \text{Tr}(\rho \hat{d}) = (\rho_{12} + \rho_{21}) \langle 1 | \hat{d} | 2 \rangle \quad (\text{A.4})$$

where $\langle 1 | \hat{d} | 2 \rangle$ denotes the dipole matrix element. The energy shift is then given by:

$$\Delta\omega = -|\mathbf{E}| \langle \hat{d} \rangle = \frac{\Delta\Omega^2}{\Omega^2/2 + \Delta^2 + \gamma^2/4} = -\frac{1}{2}\alpha|\mathbf{E}|^2 \quad (\text{A.5})$$

The scattering rate is simply given by:

$$\Gamma = \gamma \rho_{22} = \frac{\gamma \Omega^2}{2\Omega^2 + 4\Delta^2 + \gamma^2} \quad (\text{A.6})$$

List of Figures

3.1	Fluorescence of the blue MOT	10
3.2	Experimental sequence	11
4.1	Schematic of a Fabry-Perot cavity	14
4.2	Laguerre Gauss modes.	15
4.3	Cavity reflection coefficient and its imaginary part	16
4.4	Cavity ring down	18
4.5	PDH error signal	20
4.6	Optics setup and electronics for PDH locking	22
4.7	PSD of the PDH error signal	25
4.8	Beat note of α laser with the frequency comb	26
4.9	Setup for FNC and intensity stabilization.	28
4.10	PSD of the FNC beat note	29
4.11	Side band suppression for FNC	30
4.12	Allan deviation of relative fractional instability between remote locations and FNC	31
4.13	Frequency comb in temporal and frequency domain	33
4.14	CEO signal	36
4.15	Comparison between different CEO subtraction schemes	37
5.1	Lambda scheme	41
5.2	Autler-Townes peak locations	42
6.1	Lattice light shift near the $1u(20,1)$ resonance.	48
6.2	Magic wavelength	49
6.3	Narrow two-photon resonance	52
7.1	Rabi oscillations between $X(-1,0)$ and $X(6,0)$	55
7.2	Lifetime measurement of $X(6,0)$	56
8.1	Heat map of transition strengths	60
A.1	Picture of the ECDL housing	63

List of Tables

4.1	Specifications of the Fabry-Perot cavity	17
4.2	Explanation of different CEO subtraction schemes	37
5.1	Comparison between experimental and theoretical binding energies for the deeply bound ground states $X(v, 0)$	45
6.1	Comparison between experiment and theory for the transitions $X(6, 0) \leftrightarrow$ $1_u(v', 1)$	50
A.1	Parts list for ECDL	64

Bibliography

- [1] C. Patrignani, P. D. Group, et al. "Review of particle physics." In: *Chinese physics C* 40.10 (2016), p. 100001.
- [2] R. Adam, P. Ade, N. Aghanim, Y. Akrami, M. Alves, F. Argüeso, M. Arnaud, F. Arroja, M. Ashdown, J. Aumont, et al. "Planck 2015 results-I. Overview of products and scientific results." In: *Astronomy & Astrophysics* 594 (2016), A1.
- [3] G. Aad, T. Abajyan, B. Abbott, J. Abdallah, S. A. Khalek, A. Abdelalim, O. Abdinov, R. Aben, B. Abi, M. Abolins, et al. "Observation of a new particle in the search for the Standard Model Higgs boson with the ATLAS detector at the LHC." In: *Physics Letters B* 716.1 (2012), pp. 1–29.
- [4] M. Safranova, D. Budker, D. DeMille, D. F. J. Kimball, A. Derevianko, and C. W. Clark. "Search for new physics with atoms and molecules." In: *Reviews of Modern Physics* 90.2 (2018), p. 025008.
- [5] D. Budker and M. Romalis. "Optical magnetometry." In: *Nature Physics* 3.4 (2007), p. 227.
- [6] B. P. Abbott, R. Abbott, T. Abbott, M. Abernathy, F. Acernese, K. Ackley, C. Adams, T. Adams, P. Addesso, R. Adhikari, et al. "Observation of gravitational waves from a binary black hole merger." In: *Physical review letters* 116.6 (2016), p. 061102.
- [7] A. D. Ludlow, M. M. Boyd, J. Ye, E. Peik, and P. O. Schmidt. "Optical atomic clocks." In: *Reviews of Modern Physics* 87.2 (2015), p. 637.
- [8] T. Nicholson, S. Campbell, R. Hutson, G. Marti, B. Bloom, R. McNally, W. Zhang, M. Barrett, M. Safranova, G. Strouse, et al. "Systematic evaluation of an atomic clock at 2×10^{-18} total uncertainty." In: *Nature communications* 6 (2015), p. 6896.
- [9] J.-P. Uzan. "The stability of fundamental constants." In: *Comptes Rendus Physique* 16.5 (2015), pp. 576–585.
- [10] J.-P. Uzan. "Varying constants, gravitation and cosmology." In: *Living Reviews in Relativity* 14.1 (2011), p. 2.

Bibliography

- [11] N. Huntemann, B. Lipphardt, C. Tamm, V. Gerginov, S. Weyers, and E. Peik. "Improved limit on a temporal variation of m_p/m_e from comparisons of Yb+ and Cs atomic clocks." In: *Physical review letters* 113.21 (2014), p. 210802.
- [12] V. Flambaum and M. Kozlov. "Enhanced sensitivity to the time variation of the fine-structure constant and m_p/m_e in diatomic molecules." In: *Physical review letters* 99.15 (2007), p. 150801.
- [13] D. DeMille, S. Sainis, J. Sage, T. Bergeman, S. Kotochigova, and E. Tiesinga. "Enhanced sensitivity to variation of m_e/m_p in molecular spectra." In: *Physical review letters* 100.4 (2008), p. 043202.
- [14] T. Zelevinsky, S. Kotochigova, and J. Ye. "Precision test of mass-ratio variations with lattice-confined ultracold molecules." In: *Physical Review Letters* 100.4 (2008), p. 043201.
- [15] S. Kotochigova, T. Zelevinsky, and J. Ye. "Prospects for application of ultracold Sr₂ molecules in precision measurements." In: *Physical Review A* 79.1 (2009), p. 012504.
- [16] G. Herzberg. *Molecular spectra and molecular structure*. Vol. 1. Read Books Ltd, 2013.
- [17] W. Skomorowski, F. Pawłowski, C. P. Koch, and R. Moszynski. "Rovibrational dynamics of the strontium molecule in the A Σ u+ 1, c3Π u, and a Σ u+ 3 manifold from state-of-the-art ab initio calculations." In: *The Journal of chemical physics* 136.19 (2012), p. 194306.
- [18] W. Skomorowski, R. Moszynski, and C. P. Koch. "Formation of deeply bound ultracold Sr₂ molecules by photoassociation near the ¹S + ³P₁ intercombination line." In: *Physical Review A* 85.4 (2012), p. 043414.
- [19] C. B. Osborn. *The physics of ultracold Sr₂ molecules: optical production and precision measurement*. Columbia University, 2014.
- [20] K. M. Jones, E. Tiesinga, P. D. Lett, and P. S. Julienne. "Ultracold photoassociation spectroscopy: Long-range molecules and atomic scattering." In: *Reviews of Modern Physics* 78.2 (2006), p. 483.
- [21] G. Reinaudi, C. Osborn, M. McDonald, S. Kotochigova, and T. Zelevinsky. "Optical Production of Stable Ultracold ⁸⁸Sr₂ Molecules." In: *Physical review letters* 109.11 (2012), p. 115303.
- [22] G. Reinaudi, C. Osborn, K. Bega, and T. Zelevinsky. "Dynamically configurable and optimizable Zeeman slower using permanent magnets and servomotors." In: *JOSA B* 29.4 (2012), pp. 729–733.

- [23] T. Ido and H. Katori. "Recoil-free spectroscopy of neutral Sr atoms in the Lamb-Dicke regime." In: *Physical review letters* 91.5 (2003), p. 053001.
- [24] B. E. Saleh, M. C. Teich, and B. E. Saleh. *Fundamentals of photonics*. Vol. 22. Wiley New York, 1991.
- [25] A. Korpel. "Acousto-optics—a review of fundamentals." In: *Proceedings of the IEEE* 69.1 (1981), pp. 48–53.
- [26] E. D. Black. "An introduction to Pound-Drever-Hall laser frequency stabilization." In: *American Journal of Physics* 69.1 (2001), pp. 79–87.
- [27] R. W. Fox, C. W. Oates, and L. W. Hollberg. 1. *Stabilizing diode lasers to high-finesse cavities*. Vol. 40. Elsevier, 2003, pp. 1–46.
- [28] Stable Laser Systems. *Fabry-Perot cavity product page*. <http://www.stablelasers.com/fabry-perot-cavities/>. Accessed July 7, 2018.
- [29] D. Hall. *The physics and technology of laser resonators*. CRC Press, 1990.
- [30] N. Wong and J. L. Hall. "Servo control of amplitude modulation in frequency-modulation spectroscopy: demonstration of shot-noise-limited detection." In: *JOSA B* 2.9 (1985), pp. 1527–1533.
- [31] Vescent Photonics Inc. *D2-125 laser servo manual*. http://www.vescent.com/manuals/doku.php?id=d2:laser_servo. Accessed July 7, 2018.
- [32] T. Okoshi, K. Kikuchi, and A. Nakayama. "Novel method for high resolution measurement of laser output spectrum." In: *Electronics letters* 16.16 (1980), pp. 630–631.
- [33] A. D. Ludlow, X. Huang, M. Notcutt, T. Zanon-Willette, S. Foreman, M. Boyd, S. Blatt, and J. Ye. "Compact, thermal-noise-limited optical cavity for diode laser stabilization at 1×10^{-15} ." In: *Optics letters* 32.6 (2007), pp. 641–643.
- [34] S. Webster, M. Oxborow, S. Pugla, J. Millo, and P. Gill. "Thermal-noise-limited optical cavity." In: *Physical Review A* 77.3 (2008), p. 033847.
- [35] L.-S. Ma, P. Jungner, J. Ye, and J. L. Hall. "Delivering the same optical frequency at two places: accurate cancellation of phase noise introduced by an optical fiber or other time-varying path." In: *Optics letters* 19.21 (1994), pp. 1777–1779.
- [36] W. Riley. *Handbook of Frequency*. NIST, 2008.
- [37] C. E. Calosso, C. Clivati, and S. Micalizio. "Avoiding aliasing in Allan variance: an application to fiber link data analysis." In: *IEEE transactions on ultrasonics, ferroelectrics, and frequency control* 63.4 (2016), pp. 646–655.

Bibliography

- [38] B. Rauf, M. Vélez López, P. Thoumany, M. Pizzocaro, and D. Calonico. "Phase noise cancellation in polarisation-maintaining fibre links." In: *Review of Scientific Instruments* 89.3 (2018), p. 033103.
- [39] J. L. Hall and N. JILA. "Defining and measuring optical frequencies: the optical clock opportunity-and more." In: *Nobel lecture* (2005), pp. 103–135.
- [40] T. W. Hansch. "Passion for precision." In: *CHEMPHYSCHM-WINHEIM*- 7.6 (2006), p. 1170.
- [41] J. Ye and S. T. Cundiff. *Femtosecond optical frequency comb: principle, operation and applications*. Springer Science & Business Media, 2005.
- [42] B. Widiyatmoko, K. Imai, M. Kourogi, and M. Ohtsu. "Second-harmonic generation of an optical frequency comb at 1.55 μm with periodically poled lithium niobate." In: *Optics letters* 24.5 (1999), pp. 315–317.
- [43] J. K. Ranka, R. S. Windeler, and A. J. Stentz. "Visible continuum generation in air-silica microstructure optical fibers with anomalous dispersion at 800 nm." In: *Optics letters* 25.1 (2000), pp. 25–27.
- [44] J. M. Dudley, G. Genty, and S. Coen. "Supercontinuum generation in photonic crystal fiber." In: *Reviews of modern physics* 78.4 (2006), p. 1135.
- [45] D. Nicolodi, B. Argence, W. Zhang, R. Le Targat, G. Santarelli, and Y. Le Coq. "Spectral purity transfer between optical wavelengths at the 10^{-18} level." In: *Nature Photonics* 8.3 (2014), p. 219.
- [46] M. Fleischhauer, A. Imamoglu, and J. P. Marangos. "Electromagnetically induced transparency: Optics in coherent media." In: *Reviews of modern physics* 77.2 (2005), p. 633.
- [47] S. H. Autler and C. H. Townes. "Stark effect in rapidly varying fields." In: *Physical Review* 100.2 (1955), p. 703.
- [48] E. Brion, L. H. Pedersen, and K. Mølmer. "Adiabatic elimination in a lambda system." In: *Journal of Physics A: Mathematical and Theoretical* 40.5 (2007), p. 1033.
- [49] A. Stein, H. Knöckel, and E. Tiemann. "The $^1\text{S} + ^1\text{S}$ asymptote of Sr_2 studied by Fourier-transform spectroscopy." In: *The European Physical Journal D* 57.2 (2010), pp. 171–177.
- [50] J. J. Sakurai and E. D. Commins. *Modern quantum mechanics, revised edition*. AAPT, 1995.
- [51] C. J. Foot. *Atomic physics*. Vol. 7. Oxford University Press, 2005.

- [52] J. C. Kangara, A. J. Hachtel, M. C. Gillette, J. T. Barkeloo, E. R. Clements, S. Bali, B. E. Unks, N. A. Proite, D. D. Yavuz, P. J. Martin, et al. "Design and construction of cost-effective tapered amplifier systems for laser cooling and trapping experiments." In: *American Journal of Physics* 82.8 (2014), pp. 805–817.
- [53] B. McGuyer, M. McDonald, G. Iwata, M. Tarallo, W. Skomorowski, R. Moszynski, and T. Zelevinsky. "Precise study of asymptotic physics with subradiant ultracold molecules." In: *Nature Physics* 11.1 (2015), p. 32.
- [54] M. G. Littman and H. J. Metcalf. "Spectrally narrow pulsed dye laser without beam expander." In: *Applied optics* 17.14 (1978), pp. 2224–2227.
- [55] K. Liu and M. G. Littman. "Novel geometry for single-mode scanning of tunable lasers." In: *Optics letters* 6.3 (1981), pp. 117–118.
- [56] H.-P. Breuer, F. Petruccione, et al. *The theory of open quantum systems*. Oxford University Press on Demand, 2002.

Erklärung

Hiermit erkläre ich, die vorliegende Arbeit selbstständig verfasst zu haben und keine anderen als die in der Arbeit angegebenen Quellen und Hilfsmittel benutzt zu haben.

Datum

Unterschrift